PACS: 61.05.C–; 61.10.Eq; 61.43.Gt;
61.46.+w; 67.30.hp; 68.08.−p; 68.37.Og; 68.43.–h; 68.47.Gh

doi: 10.15407/hftp15.01.003

V.M. Gun'ko, V.V. Turov

COLLIGATIVE PROPERTIES OF VARIOUS LIQUID BLENDS *VS.* TEMPERATURE UNDER CONFINED SPACE EFFECTS IN PORES OF DIFFERENT ADSORBENTS

Chuiko Institute of Surface Chemistry of National Academy of Sciences of Ukraine
17 General Naumov Str., Kyiv, 03164, Ukraine, E-mail: vlad_gunko@ukr.net

The temperature and interfacial behaviors of individual and mixed liquids are of importance from a practical point of view because changes in the phase state of compounds with decreasing temperature could lead to negative effects (e.g., frost damage of porous materials). However, the use of certain mixtures may prevent these negative effects due to the colligative properties of the solutions (cryscopic effects, CE) that lead to several effects including relative lowering of vapor pressure, boiling point elevation, and freezing point depression (FPD). Confined space effects (CSE) also leading to the freezing point depression can affect the colligative properties of liquid mixtures with respect to FPD. One could assume that for some systems with certain FPD due to CE for bulk solutions, there is no additivity (synergetic effect) of CSE and CE, but for others, the opposite results could be. To elucidate these interfacial phenomena, a set of liquid mixtures bound to different adsorbents could be studied using low-temperature NMR spectroscopy. The solutions included acids, bases, and salts as solutes, some liquids (e.g., dimethylsulfoxide, acetonitrile, n-decane) as co-sorbates and others (e.g., $CDCl_3$, CCl_4) as dispersion media. The adsorbents included various porous and highly disperse silicas, fumed alumina, carbons (activated carbons, graphene oxides), and porous polymers. So wide ranges of the systems studied could allow one a deeper insight into competitive or additive CSE and CE influencing the interfacial and temperature behaviors of bound liquids. The results of this analysis are of interest from both practical and theoretical points of view.

Keywords*: nanosilica, silica gel, carbon adsorbents, polymeric adsorbents, bound aqueous solutions, interfacial phenomena; confined space effect, cryoscopic effect*

INTRODUCTION

The temperature behavior of liquids bound in pores is of importance from a practical point of view, *e.g*., because increased volume of ice in comparison to liquid water can lead to frost damage of porous materials [1–3]. However, the use of water mixtures with some solutes could prevent the frost damage of the materials even at very low temperatures due to the colligative properties (CP) of the solutions freezing at lower temperatures than that of individual components. There are other practically important aspects of the interfacial phenomena related to adsorbent swelling, adsorption, evaporation, solubility and dissociation degree of solutes, *etc. vs*. temperature. The colligative properties of ideal solutions depend on a ratio of a number of solute particles to a number of solvent particles [4–7]. The CP of the mixtures lead to several effects: (i) relative lowering of vapor pressure (Raoult's law); (ii) boiling point elevation; and (iii) freezing point depression, FPD (cryoscopic effect, CE) $T_{f,s} - T_{f,b} = \Delta T_{f,CE,b} = iK_f m < 0$, where i is the Van't Hoff factor (the number of ions of a compound dissociated per formula unit), K_f is the molal freezing–point depression constant related to the solvent (*e.g*., K_f = –1.86 K/m for water and –3.9 K/m for acetic acid), m is the molality of a solute (the number of moles of a solute in a solution corresponding to 1 kg of a solvent, m = 1/0.018 mol/kg for pure water) [4–14].

Confined space effects (CSE) on liquid adsorbates located in pores also lead to FPD at $\Delta T_{f,CSE} = -k/R$ (R is the pore radius) [15–19]. The CSE could also result in a decrease in the solvent activity, and the narrower the pores the stronger the FPD and the activity diminution. The question arises with respect to the behavior of solutions (*e.g*., deep eutectic solvents, DES) in pores since both CE and CSE depend on temperature, mixture compositions, and pore sizes. For the DES, a location of the eutectic point could be strongly varied depending on the kind of solvents and solutes (Fig. 1) [20–29]. Additionally, the curves of the freezing (melting) point *vs*. the solvent/solute amounts can have several extrema

due to the reorganization of the solutions with increasing content of solutes that also depends on a kind of solutes and other factors [30–33].

Note that the weakening of hydration capacity by confinement is the internal driving force for the ion association [31]; *i.e.*, dissolution and dissociation of acids, salts, and other ion-generating solutes could decrease in pores, especially in nanopores. One could assume that the CE in pores could differ from those in the bulk solutions due to the CSE. Therefore, to analyze some aspects of the CE/CSE influence on various systems in a wide range of temperatures, a set of liquid mixtures bound to different adsorbents could be studied using low-temperature ^{1}H NMR spectroscopy and quantum chemistry methods. Additionally, for the material characterization, several methods such as the nitrogen adsorption, microscopy, and cryoporometry could be used.

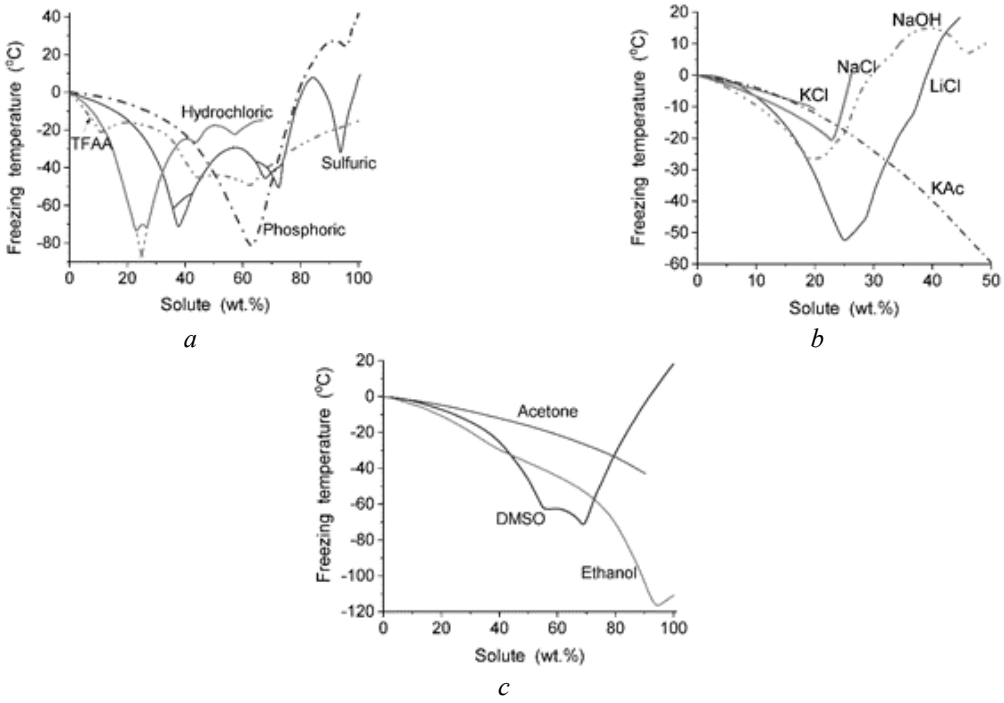

Fig. 1. Freezing temperature *vs*. solute concentration in the aqueous solutions with (*a*) acids (TFAA is trifluoroacetic acid), (*b*) salts (KAc is the salt of acetic acid) and NaOH, and (*c*) organic solvents showing complex cryoscopic effects due to the colligative properties of the solutions that result in the appearance of several eutectic points for some systems [20–29]

MATERIALS AND METHODS

Several nanosilica samples (Pilot plant of Chuiko Institute of Surface Chemistry (CISC), Kalush, Ukraine) and fumed silica OX–50 (Evonik) have been studied (Table 1) including hydrophilic fumed silica A–300 and hydrophobic functionalized fumed silica AM1. Both nanosilicas are composed of nonporous nanoparticles, NPNP (< 20 nm in size) forming aggregates (< 1 μm), agglomerates of aggregates (1–50 μm), and visible particles in the loose powders of low bulk density (ρ_b = 0.04–0.06 g/cm^3). The last three hierarchical levels of the particulate morphology could be assigned to supra–NP structures responsible for the textural porosity of the powders. To enhance the CSE, before the use of nanosilicas, they were compacted using water for A–300 (stirred and dried at 433 K for several hours, $\rho_b \approx 0.3$ g/cm^3 for hydro-compacted cA–300 and $\rho_b \approx 0.6$ g/cm^3 after stirring, *e.g.*, with NaOH) or ethanol for AM1 (stirred and dried at 373 K for 12 h and at 298 K for 18 days, ρ_b = 0.25 g/cm^3), or using others conditions of the powder compaction (*vide infra*).

Additionally, for AM1, three types of treatments were used. First, it (ethanol-compacted cAM1) was stirred with water (0.1 g water per gram of dried AM1) that results in ρ_b = 0.3 g/cm^3. Second, cAM1 was stirred with dry NaOH (for several minutes) and then with added water.

Third, cAM1 was stirred with NaOH pre-stirred with water. In all the cases, the content of NaOH (and water) was 0.1 g per gram of dry silica. These treatments provided removal of air microbubbles from wetted cAM1 (therefore, it could be wetted by bulk water). The air was removed from the treated cAM1 powder located in organic dispersion media with deuterated chloroform $CDCl_3$, dimethylsulfoxide (DMSO-d6), or their mixtures xCDCl$_3$/yDMSO (x and y correspond to 1:1, 1:2, 1:3, and 3:1). These systems, as well as others based on nanooxides, could be considered as nano-heterogeneous ones without the formation of separated phases; *i.e.*, they are macro-homogeneous. Note that in the case of silica gels, activated carbons, and other adsorbents composed of porous micro/macroglobules, it is impossible to prepare similar nano-heterogeneous and macro-homogeneous systems. A small amount of water bound in the silica/NaOH systems prevents dissolving of the surface silica layers because clustered water located in voids between NPNP is a poor solvent for NaOH. Additionally, NaOH could be dissolved in water at the ratio of *ca.* 1/1 w/w at 293–298 K. However, the low–temperature ^{1}H NMR spectroscopy measurements were carried out at lower temperatures (215–287 K) using fresh samples. Therefore, one could assume that the damages of the surface functionalities of AM1 (or dissolution of surface A–300 layers) due to interaction with NaOH/water (1:1) are small upon the NMR investigations at low temperatures [16, 34–36].

Table 1. Textural characteristics of used adsorbents: silica gels (200DF, Si–x), ordered mesoporous silicas (MCM–48, SBA–15), precipitated silica (Syloid 244), fumed silicas (A–300, AM1 (A–200 with dimethylsilyl groups), OX–50), activated carbons (C–86 and C–47 with 86 % and 47 % burn–off), polymers (Lichrolut EN, polymethylsiloxane (PMS))

Sample	S_{BET}, m^2/g	S_{nano}, m^2/g	S_{meso}, m^2/g	S_{macro}, m^2/g	S_{NLDFT}, m^2/g	V_p, cm^3/g	V_{nano}, cm^3/g	V_{meso}, cm^3/g	V_{macro}, cm3/g	$\langle R_V \rangle$, nm	$\langle R_S \rangle$, nm
200DF	540	429	111	0	496	0.336	0.244	0.092	0	0.92	0.87
Silicalite	448	355	93	0	675	0.231	0.167	0.064	0	0.89	0.84
Si–40	732	45	687	0	617	0.636	0.009	0.627	0	2.21	2.04
Si–60	369	10	359	0	357	0.753	0.002	0.743	0	4.64	4.35
Si–100	350	74	276	0	344	1.225	0.041	1.184	0	7.24	5.03
MCM–48	1019	51	967	0.3	1024	0.702	0.022	0.672	0.008	2.50	1.61
SBA–15	832	150	680	2	902	1.333	0.065	1.224	0.044	6.09	3.13
Syloid–244	336	39	291	6	335	1.591	0.022	1.457	0.112	11.89	8.24
A–300	294	44	229	16	289	0.850	0.023	0.567	0.259	20.41	6.14
AM1	178	0	153	25	133	0.466	0	0.228	0.238	32.3	12.5
OX–50	54	34	14	6	39	0.144	0.010	0.042	0.092	39.72	7.54
C–86	3463	3104	354	5	2840	2.321	1.473	0.644	0.204	8.31	0.89
C–47	1648	1490	143	15	1698	1.876	0.713	0.737	0.428	14.21	1.36
LichrolutEN	1512	1064	448	0.2	1309	0.827	0.426	0.393	0.008	2.16	0.95
PMS	507	2	504	1	471	1.320	0.002	1.304	0.014	6.08	5.28
Stirred PMS	572	1	558	13	581	2.604	0.001	2.248	0.355	16.86	9.42

Note. The values V_{nano} and S_{nano} were calculated by integration of the PSD functions $f_V(R)$ and $f_S(R)$, respectively, at 0.35 nm < R < 1.0 nm, V_{meso} and S_{meso} at 1 nm < R < 25 nm, and V_{macro} and S_{macro} at 25 nm < R < 100 nm. $\langle R_X \rangle = \int_{R_{min}}^{R_{max}} R f_X(R) dR \,/\, \int_{R_{min}}^{R_{max}} f_X(R) dR$ are the average pore radii with respect to the pore volume (V) and surface area (S)

Additionally, silica gels Gasil 200DF (Crosfield), Si–40, Si–60, and Si–100 (Merck), ordered mesoporous silicas MCM–48 and SBA–15 (CISC), silicalite (ZSM5–like structure) (CISC); polymeric Lichrolut EN (Merck); and activated carbons (AC) C–47 and C–86 (MAST Carbon International Ltd., UK) were used as initial materials [16].

Commercial initial hydrogel of polymethylsiloxane (Enterosgel, $C_{PMS} \approx 7$ wt. %,

purity > 99.5 %, Kreoma–Pharm, Ukraine) synthesized using methyltrichlorosilane was used as received. PMS in Enterosgel is hydrophilic due to residual silanols. After drying of Enterosgel at 293 K for a constant weight, residual water amount is small (*ca*. 0.7 wt. %) and the material (PMS) has hydrophobic properties [37, 38]. After stirring of this PMS with water (1/1 g/g, 293 K, 20 min) under certain mechanical loading (hydrocompaction, cPMS), it becomes again hydrophilic.

Samples with salts (LiCl, NaCl, and KCl, Merck) mixed with A–300 or PMS with a weight ratio of 3/1, 1/1, 1/3, and 1/6 w/w were prepared by grinding in a porcelain mortar (20 min, 293 K). For ^{1}H NMR measurements at different temperatures, the samples were placed into 5 mm NMR ampoules, and after addition of certain amounts of water or/and *n*–decane, hydrophobic liquids ($CDCl_3$ or CCl_4, ~3 g) were added to form the dispersion media. Certain amounts of acetonitrile or/and TFAA were added into the dispersion media for some samples. Salts located at the interfaces of solid/bound water (or/and decane)/dispersion medium could be partially dissolved or represent undissolved micro/nanoparticles, which can strongly affect the interfacial and temperature behaviors of bound liquids. Anions Cl^- and cations K^+ are chaotropic, but cations Li^+ and Na^+ are kosmotropic, and they can strongly and differently affect the water properties. The cation effects on water increase with decreasing cation size and depend strongly on the degree of hydration, and the Jones–Dole viscosity (*B*) coefficient is equal to –0.007 (K^+, Cl^-), 0.086 (Na^+), and 0.15 (Li^+) [16, 19, 39–42].

The low–temperature ^{1}H NMR spectra of static samples were recorded using a Varian 400 Mercury spectrometer (magnetic field 9.4 T) utilizing 60° or 90° pulses of 1–3 μs duration [16]. Each spectrum was recorded by co-addition of eight scans with a 2 s delay between each scan. Relative mean errors were less than ±10 % for ^{1}H NMR signal intensity for overlapped signals, and ±5 % for single signals. Temperature control was accurate and precise to within ±1 K. The accuracy of integral intensities was improved by compensating for phase distortion and zero–line nonlinearity with the same intensity scale at different temperatures. To prevent supercooling, the spectra were recorded starting at 200–215 K for samples precooled to this temperature for 10 min. Samples were heated to 280–290 K at a rate of 5 K/min with steps ΔT = 2–15 K, and maintained at a fixed temperature for 5 min for data acquisition at each temperature. Note that signals of immobile (frozen) molecules and functionalities of solid particles were not registered in the ^{1}H NMR spectra of static samples due to a narrow bandwidth (20 kHz) and a large difference in the transverse relaxation time of mobile and immobile phases [16].

Changes in the process of water freezing are determined by a decrease in the Gibbs free energy (ΔG) of water due to adsorption interactions. This could be estimated from the equation for ΔG_{ice} *vs.* temperature for ice

$$\Delta G_{ice} = 0.0295 - 0.0413\Delta T + 6.64369\times10^{-5}(\Delta T)^2 + 2.27708\times10^{-8}(\Delta T)^3, \text{ (kJ/mol)} \quad (1)$$

where $\Delta T = 273.16 - T$ at $T \le 273.15$ K. For the temperature range of 215–273 K, a simpler equation could be also used

$$\Delta G_{ice} = -0.036\Delta T. \quad (2)$$

Changes in the Gibbs free energy (ΔG) of bound water *vs*. the amounts of unfrozen water (C_{uw} in mg of water per gram of dry sample with the average errors of *ca*. ±5 %) were determined at T = 200–273 K using tabulated $\Delta G(T)$ data for ice (the errors are negligibly small). The area under the $\Delta G(C_{uw})$ curve (obtained from the dependences of ΔG and C_{uw} on temperature) determines the surface Gibbs free energy γ_S (the modulus of overall changes in the Gibbs free energy of bound water due to interaction with a surface) [16]

$$\gamma_S = -A \int_0^{C_{uw}^{max}} \Delta G(C_{uw}) dC_{uw}, \quad (3)$$

where C_{uw}^{max} is the total amount of unfrozen water at T = 273 K, and A (> 0) is a constant dependent on the type of units used in eq. (3). To take into account the amounts of unfrozen water bound in different samples, the normalized values $\gamma_S^* = \gamma_S/(C_{uw}^w + C_{uw}^s)$, where C_{uw}^w and C_{uw}^s are the amounts of weakly bound water, WBW (unfrozen at 265 K < T < 273.15 K) and strongly bound water, SBW (unfrozen at T < 265 K), respectively, were also computed.

Water can be frozen/melted in narrower pores (or voids between nanoparticles) at lower

temperatures (T < 273 K) as described by the Gibbs–Thomson relation for the freezing/melting point depression for liquids confined in cylindrical pores at radius R [16–19]

$$\Delta T_m = T_{m,\infty} - T_m(R) = -\frac{2\sigma_{sl}T_{m,\infty}}{\Delta H_f \rho R} = \frac{k_{GT}}{R}, \qquad (4)$$

where $T_m(R)$ is the melting temperature of ice in cylindrical pores of radius R, $T_{m,\infty}$ the bulk melting temperature, ΔH_f the bulk enthalpy of fusion, ρ the density of the solid, σ_{sl} the energy of solid–liquid interaction, and k_{GT} is the Gibbs–Thomson constant (here k_{GT} = 40–90 K nm varied for different systems: polymers < silicas < carbons). Eq. (4) was used to determine the cluster size distributions (CSD) ($f_V(R) = dV_{uw}(R)/dR$) of bound water unfrozen at T < 273 K (the average errors are smaller than ±10 %). The CSD were converted into incremental CSD (ICSD) $\Phi_V(R_i) = (f_V(R_{i+1}) + f_V(R_i))(R_{i+1} - R_i)/2$ at $\sum\Phi_{V,i}(R) = V_{uw}$. Integration of the $f_V(R)$ and $f_S(R)$ functions at 0.2 nm < R < 1 nm, 1 nm < R < 25 nm, and 25 nm < R < 100 nm gives the volume and the specific surface area of nano–, meso– and macropores, respectively, contacted with unfrozen water (or aqueous solution). The specific surface area (S_{uw}) of adsorbents in contact with unfrozen bound water (assuming for simplicity that the density of this water ρ_{uw} = 1 g/cm^3) can be determined from the amount of this water C_{uw}^{max} (estimating pore volume as $V_{uw} = C_{uw}^{max}/\rho_{uw}$) at T = 273.15 K and pore size distribution $f(R)$ with a model of cylindrical pores [16]

$$S_{uw} = \frac{V_{uw}}{2R_{av}} = \frac{2C_{uw}^{max}}{\rho_{uw}} \int_{R_{min}}^{R_{max}} f(R)dR \Big/ \int_{R_{min}}^{R_{max}} f(R)RdR, \quad (5)$$

where R_{min} and R_{max} are the minimal and maximal radii of pores filled by unfrozen water, respectively. The average melting temperature $<T_m>$ was calculated using formula [16]

$$<T_m> = \int_{T_{min}}^{T_0} TC_{uw}(T)dT \Big/ \int_{T_{min}}^{T_0} C_{uw}(T)dT, \qquad (6)$$

where T_0 = 273.15 K, and T_{min} is the temperature corresponding to C_{uw} = 0.

The chemical shift of the proton resonance ($\delta_H(T)$ function) depends on the number of possible configurations of the water molecules in the hydrogen bonds network (HBN) strongly affected by hydrophilic and hydrophobic or mosaic functionalized surroundings and dispersion media [43]. Considering that, this number is inversely proportional to the average number of the hydrogen bonds $<n_{HB}>$, according to the hydrogen bond network entropy definition $S \approx -k_B \ln n_{HB}$ [43]. Therefore, the temperature derivative of the measured fractional chemical shift

$$-\left(\frac{\partial \ln \delta(T)}{\partial T}\right)_p = -\left(\frac{\partial \ln < n_{HB} >}{\partial T}\right)_p \approx \left(\frac{\partial S}{\partial T}\right)_p \qquad (7)$$

should be proportional to the constant pressure specific heat $C_P(T)$ ($C_P = T(\partial S/\partial T)_P$). This aspect was analyzed in detail elsewhere [43]. One could assume that the function $s(T) = -T(\partial(\ln\delta(T))/\partial T)_P$ could demonstrate a different behavior for weakly (WAW) and strongly (SAW) associated waters, which are characterized by different δ_H values of 1–2 and 3–6 ppm, respectively [16].

To analyze the textural characteristics of A–300 and AM1 (Table 1) degassed at 473 and 373 K, respectively, for several hours (as well as for other adsorbents), low–temperature (77.4 K) nitrogen adsorption–desorption isotherms were recorded using a Micromeritics ASAP 2420 or ASAP 2405N adsorption analyzer. The specific surface area (Table 1, S_{BET}, average errors of *ca.* 10 %) was calculated according to the standard BET method [44]. The total pore volume (V_p, the errors are small but could be larger if the condensation on the outer surface is not considered that is checked on the analysis of the isotherm shape) was evaluated from the nitrogen adsorption at $p/p_0 \approx$ 0.98–0.99, where p and p_0 denote the equilibrium and saturation pressure of nitrogen at 77.4 K, respectively [45].

The nitrogen desorption data were used to compute the pore size distributions (PSD, differential $f_V(R) \sim dV_p/dR$ and $f_S(R) \sim dS/dR$) using the density functional theory (DFT) method (molecular DFT) with a self–consistent regularization (SCR) procedure under non-negativity condition ($f_V(R) \geq 0$ at any pore radius R) at a fixed regularization parameter α = 0.01. A complex pore model was applied with cylindrical (C) pores in silica and voids (V) between spherical silica NPNP packed in random aggregates (CV/SCR method) and also slitshaped pores for

carbons and polymers (SCV/SCR) [46]. The differential PSD with respect to the pore volume $f_V(R) \sim dV/dR$, $\int f_V(R)dR \sim V_p$ were re-calculated into incremental PSD (IPSD) at $\Phi_V(R_i) = (f_V(R_{i+1}) + f_V(R_i))(R_{i+1} - R_i)/2$ at $\sum\Phi_V(R_i) = V_p$). The $f_V(R)$ and $f_S(R)$ functions were also used to calculate contributions of nanopores (V_{nano} and S_{nano} at radius in the range of 0.35 nm < $R \le$ 1 nm), mesopores (V_{meso} and S_{meso} at 1 nm < $R \le$ 25 nm), and macropores (V_{macro} and S_{macro} at 25 nm < $R \le$ 100 nm) [46]. Additionally, the non-local density functional theory (NLDFT, Quantachrome software, with an equilibrium model of cylindrical pores in silica or slitshaped/cylindrical pores in carbons) method was used to calculate the differential PSD. The textural characteristics (Table 1) show that the silicas represent rather meso/macroporous materials since contribution of nanopores into the pore volume is about 1–2 % and about 20 % to the specific surface area.

Transition electron microscopy (TEM) images were recorded using a TECNAI G2 F30 microscope (FEI–Philips, Holland) and JEOL JEM–2100F (Japan) at an operating voltage of 300 kV. A dried sample was added to acetone (chromatographic grade) and sonicated to form uniform suspension. Then a suspension drop was deposited on a copper grid with a thin carbon film. After evaporation of acetone, nanostructured particles remained on the film were investigated.

Scanning electron microscopy (SEM) equipment (FE–SEM, Hitachi S–4700, Tokyo, Japan, operating voltage V = 15 kV, magnify-cation of ×5000–100000; QuantaTM 3D FEG, FEI, USA, V = 5–30 kV; and Zeiss Gemini 300, Carl ZEISS, V = 0.02 – 30 kV) was used to analyze the morphology. Nanosilicas studied are characterized by a hierarchical particulate morphology with spherical–like nonporous nanoparticles (NPNP) of *ca*. 10 nm in diameter forming aggregates (typically < 1 μm) and agglomerates of aggregates (> 1 μm). Agglomerates form visible loose particles.

Atomic Force Microscopic (AFM) images were obtained by means of a NanoScope III (Digital Instruments, USA) apparatus using a tapping mode AFM measurement technique. Before AFM scanning, powder samples of fumed oxides were slightly smoothed by hand pressing using a glass plate, which does not affect the structure of primary and secondary particles, changing only the structure of visible flocks.

Quantum chemical calculations using density functional theory (DFT) method (electronic DFT) were carried out using a hybrid functional ωB97X–D with the cc–pVDZ basis set or B3LYP/6–31G(d,p) with the Gaussian 16 C.02 [47] or GAMESS 2023 R2 [48] program suits. The solvation effects were analyzed using the solvation method SMD [49] implemented in the Gaussian and GAMESS programs. To compute the Gibbs free energy of solvation (subscript s), $\Delta G_s = G_l - G_g$, where G_l and G_g are the Gibbs free energies of a molecule free or bound to silica cluster in the liquid (subscript l) and gas (g) media, respectively. The calculations were performed taking into account zero–point and thermal corrections to the Gibbs free energy in the gas phase and for solved molecules and silica clusters with the geometry optimized using ωB97X–D/cc–pVDZ. The NMR spectra were calculated using the gauge–independent atomic orbital (GIAO) method calculated with or without the SMD method. Large cluster models were calculated using the PM7 method (MOPAC, ver. 22.1) (as a whole the average errors in the PM7 method results are similar to that of *ab initio* calculations with 6-31G(d) basis set) [50]. Preparation of initial cluster/molecular structures and visualization of the calculation results were carried out using several programs [51–54].

RESULTS AND DISCUSSION

The pore size distributions (PSD) (as the main characteristic of any adsorbent [55–63]) of the selected silica, carbon, and polymeric adsorbents (Fig. 2) and other textural characteristics (Table 1) show that the studied adsorbents are very different with respect to the particulate morphology (see inserts with microscopic images in several Figures) and texture. They are characterized by various contributions of nano-, meso-, and macro-pores, low and high specific surface area (SSA, Table 1, S_{BET}), pore volume (V_p), and average pore radii ($<R_v>$, $<R_S>$). One could assume that a wide set of samples will provide a more comprehensive study of the CSE/CE influence (including CSE inhibition of CE) on the temperature behavior of individual and mixed liquids bound to various adsorbents located in different dispersion media studied using the low–temperature ^{1}H NMR spectroscopy of static samples in a broad temperature range.

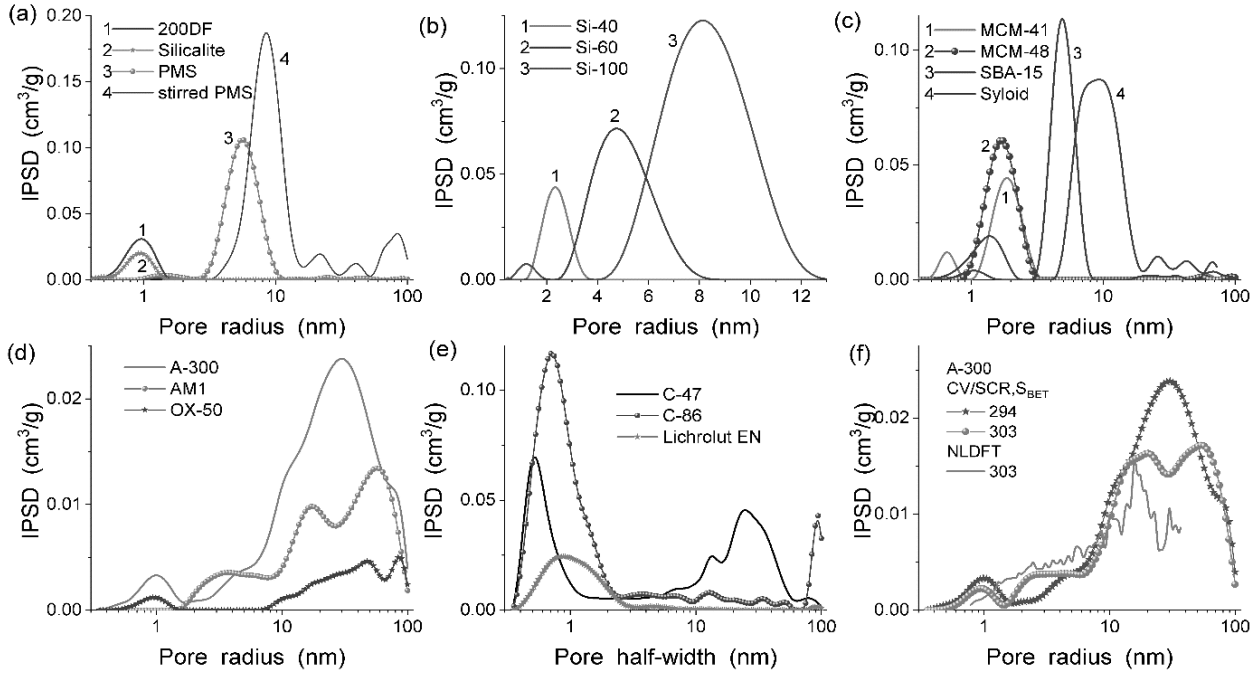

Fig. 2. Incremental pore size distributions for studied adsorbents (SCV/SCR DFT method)

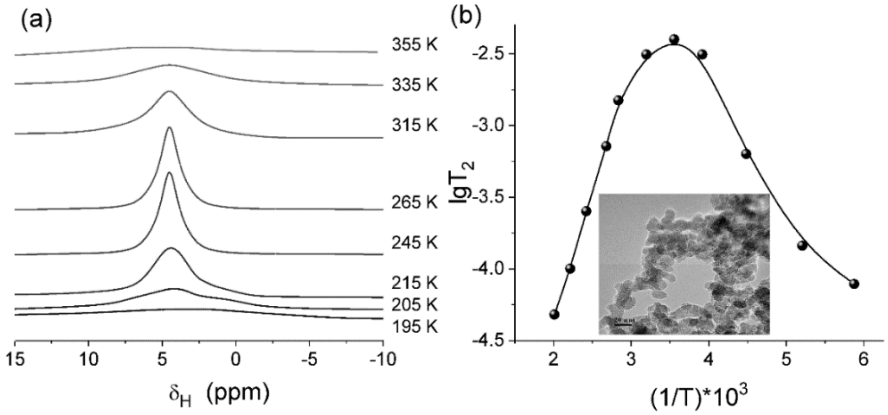

Fig. 3. (*a*) ^{1}H NMR spectra of water adsorbed onto A–300 from air and (*b*) its temperature dependence (lgT_2 *vs* 1/T) of the transversal relaxation time; insert: TEM image of A–300 (scale bar 20 nm) [16]

The NMR spectral characteristics of water bound to a nanosilica [16, 64–67] surface could be affected by the proton exchange reactions between silanols and water molecules. A large difference (two–three orders of magnitude) in transversal relaxation time of protons of the silanols and bound mobile water molecules can lead to a significant broadening of signals of both silanols and adsorbed water even in the case of a small rate of the proton exchange (cross-relaxation effect) [16]. To analyze this effect, the temperature dependences of the ^{1}H NMR band shape and transversal relaxation time (T_2) were studied for nanosilica A–300 hydrated in air (Fig. 3). The signal width decreases with increasing temperature from 195 to 265 K (Fig. 3 *a*) and then it increases and signal is not observed at T > 355 K in the high-resolution spectra. The $T_2(1/T)$ function has an inflection point at 265 K. Signal broadening (*i.e.,* a decrease in the T_2 value) with decreasing temperature to 265 K is due to a decrease in the proton exchange rate and the molecular mobility of adsorbed water at lower temperatures. In the first approximation, the slope ratio of the ln$T_2(1/T)$ curve determines the activation energy of self-diffusion of adsorbed

water molecules (to the right of the maximum, $E_a \approx 7$ kJ/mol) and the activation energy of the proton exchange reaction between water molecules and silanols (to the left of the maximum, $E_a = 13.3$ kJ/mol) [16]. One could assume on the basis of these results (Fig. 3) that the cross-relaxation becomes especially significant for water bound to nanosilica at $T > 270$ K. In the case of the aqueous suspensions of nanosilicas, the amounts of structured water in the interfacial layer but unbound directly to the silica surface are much larger (1–2 orders of magnitude) than in the case of weakly hydrated silica powder (< 5 wt. %). Therefore, contribution of water molecules participating in the proton exchange reactions with silanols to the total width of signal is low in the suspensions even at $T < 273$ K because of a significant amount of bound unfrozen water in a relatively thick adsorption layer. Thus, the cross-relaxation effect can be ignored for the frozen aqueous suspensions of nanosilicas because of two mentioned effects at low temperatures and at T close to 270–273 K. Additionally, the use of a relatively narrow bandwidth (20 kHz) and a large difference in the transverse relaxation time of mobile and immobile phases allow one to record the spectra only of mobile phases [16].

Table 2. Characteristics of nanosilica samples (first series) with low hydrophilicity

Sample	ρ_b (g/dm^3)	S_{BET} (m^2/g)	V_p (cm^3/g)	$C_{w,105}$ (wt%)	$C_{w,900}$ (wt%)
A–150	37	144	0.261	1.0	1.1
A–200	49	206	0.411	1.0	0.9
A–300	46	337	0.608	1.2	1.0
A–380	42	381	0.667	1.4	1.0

Note. $C_w = C_{w,105} + C_{w,900}$; $C_{w,105}$ is the amount of water desorbed on heating at $T < 105$ °C, $C_{w,900}$ is the amount of water desorbed at $105 < T < 900$ °C

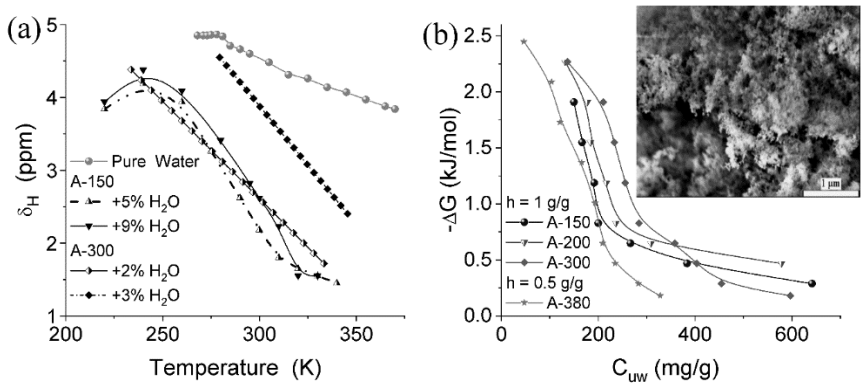

Fig. 4. (*a*) Dependence of the chemical shift δ_H vs. temperature for differently hydrated nanosilicas A–150 and A–300 and pure water; (*b*) relationship between the amounts of unfrozen water (C_{uw}) and changes in the Gibbs free energy of bound water for various nanosilicas (insert: SEM image of A–300, scale bar 1 μm)

Changes in the SSA value and amount of surface hydroxyls (Table 2) affect the characteristics of bound water such as the $\delta_H(T)$ functions (Fig. 4 *a*) and changes in the Gibbs free energy (ΔG) of bound water *vs*. the amounts of unfrozen water ($C_{uw}(T)$) at $T < 273$ K (Fig. 4 *b*). WAW ($\delta_H = 1.5$ ppm) and SAW (2.8–4.8 ppm) are observed for weakly ($h = 50$ mg/g) hydrated nanosilica A–300 in both nonpolar CCl_4 and weakly polar $CDCl_3$ media (Fig. 5 *a*, *b*). SAW and WAW demonstrate a typical dependence of δ_H on temperature since it increases or remains constant, respectively. Addition of 10 or 20 % acetonitrile to chloroform enhances contribution of WAW (1.3 ppm), and a portion of water dissolved in CD_3CN (2.5–3 ppm), as well as SAW (3.5–4 ppm) (Fig. 5 *c*–*f*). CH_3CN as an admixture in CD_3CN gives signal at ~2 ppm. At 290 K, only one broad signal is observed due to increased efficiency of exchange processes with increasing temperature. In pure acetonitrile (Fig. 5 *e*), two signals of water (2.5–3 ppm) and CH_3CN (2 ppm) are observed. At $T < 240$ K,

intensity of both signals strongly decreases due to freezing of acetonitrile.

Addition of DCl (transformed into HCl due the proton exchange reactions with water or silanols) leads to the downfield displacement of signals (Fig. 5 *f*) that is typical effect for strong acidic solutions. This effect is stronger at lower temperatures because of concentrating of dissolved acid since ice is much pure than the acid solution. However, even at 200 K, the δ_H values are lower (6–7 ppm) than that for individual concentrated HCl solution (9.5 ppm, Fig. 6 *a*) unfrozen due to the CE. This result can be explained by lower activity of bound water (additionally, the water amount is low in the system) due to the CSE than that of the bulk water. In other words, HCl/DCl forms bound clusters with a low content of water; therefore, water dissolves a small amount of the acid (dissociated). Signals of the acidic solution become lower toward 200 K. Thus, there is no the synergetic effects of CSE + CE, since at $T < 230$ K $\approx T_{f,CE,b}$ (for used water and HCl concentrations), signal intensity significantly decreases (Fig. 5 *f*) similar to water without solutes (Fig. 5 *a*) in contrast to the individual concentrated solution (Fig. 6 *a*, HCl).

Addition of DMSO, a stronger electron–donor than acetonitrile, to chloroform leads to the significant CE (Fig. 5 *g–i*). The ^{1}H NMR spectra shape (Fig. 5 *g*) is similar to that with acetonitrile (Fig. 5 *e*); however, the δ_H values for water are larger (3.5–4.5 ppm, SAW) in the $CDCl_3$–DMSO medium than in CD_3CN. A weak signal of WAW is observed at 1.5 ppm. Addition of DCl/D_2O (Fig. 5 *h*) causes splitting of the water signal into two signals with downfield shifting with lowering temperature. With increasing contents of water and acid (Fig. 5 *i*), the δ_H values increase because the activity of water (as a solvent) increases and it can dissolve a greater amount of HCl/DCl. However, the synergetic effects of CSE + CE are practically absent due to decreased activity of bound water as a solvent.

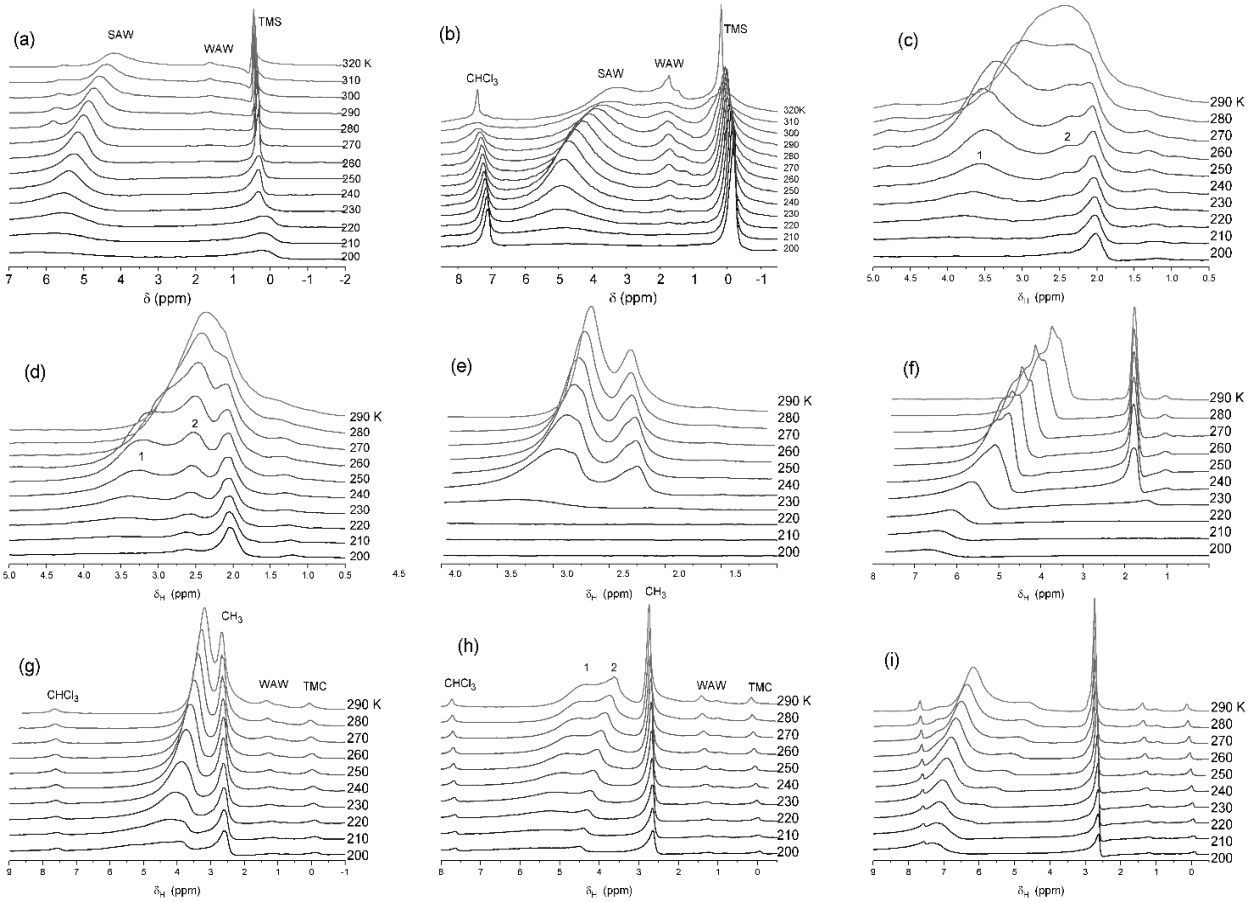

Fig. 5. ^{1}H NMR spectra of water at h = (*a–e*, *g*) 50 mg/g, (*f*, *h*) 88 mg/g, and (*h*) 88 mg/g bound to A–300 in (*a*) CCl_4 or (*b*) $CDCl_3$ + (*c*) 10 % or (*d*) 20 % CD_3CN; (*e*, *f*) CD_3CN with addition of (*f*) DCl (44 mg/g); (*g*) in $CHCl_3$ with addition of HCl (*h*) 44 and (*i*) 60 mg/g, and in $CDCl_3$ + 15 % $(CD_3)_2SO$

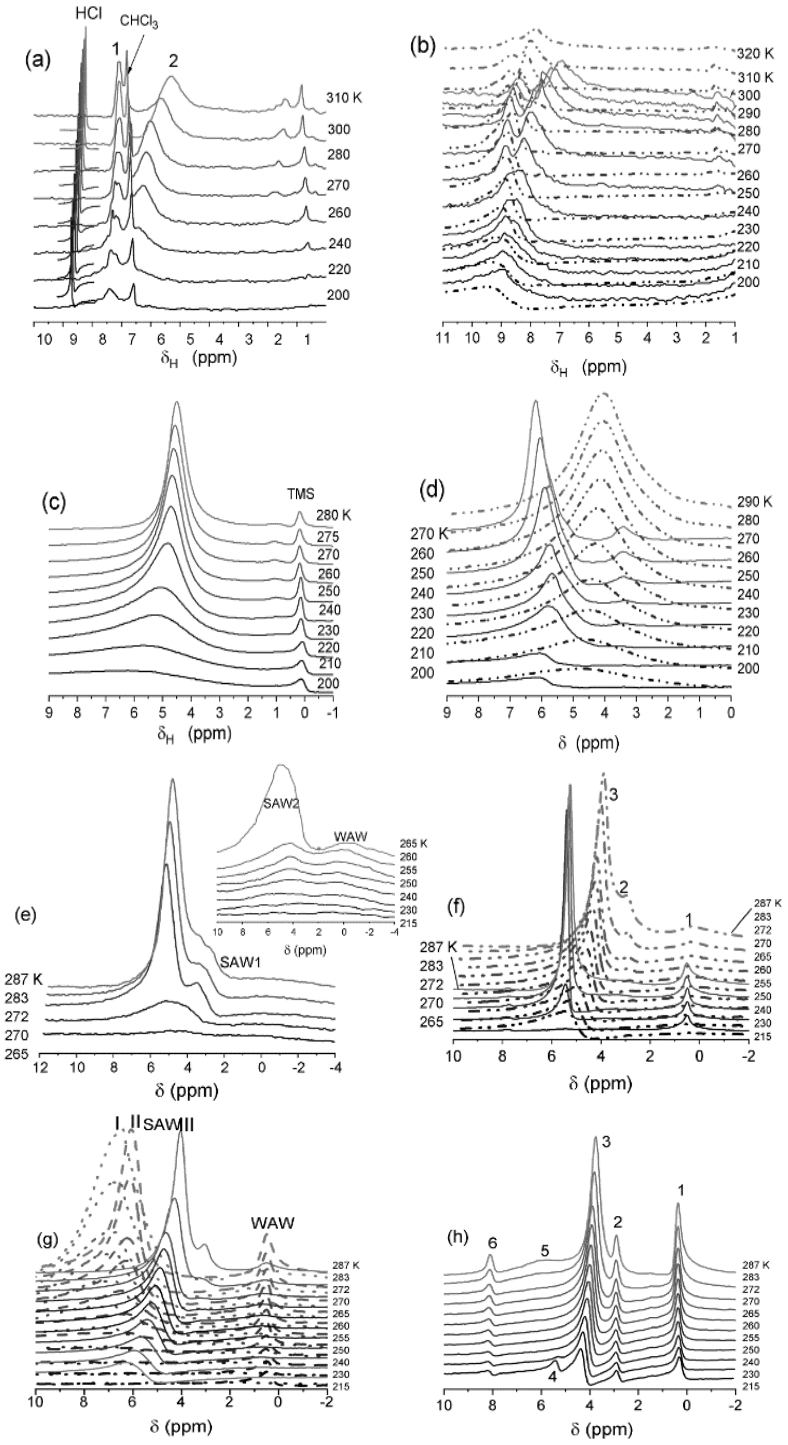

Fig. 6. ^{1}H NMR spectra of (*a*) 36 % hydrochloric acid (narrow signal at 9.0–9.4 ppm), hydrochloric acid and water bound to (*a*, *b*) initial and (*c*) cA–300 in (*a*) $CDCl_3$ or (*b–d*) CCl_4; (*a*, *b* – solid lines, *c*) 38 mg/g H_2O and 44 mg/g HCl, (*b* – dotted–dashed lines) 140 mg/g H_2O and 120 mg/g HCl; (*d*) weakly hydrated solid H_3PO_3 alone (solid lines, h = 0.07 g/g, in air) and bound to A–300/H_3PO_4 = 4/1 at h = 100 mg/g in CCl_4 medium (dotted–dashed); cAM1/water (h = 0.1 g/g) in different media: (*e*) air, (*f*) $CDCl_3$ (solid lines) and DMSO–d6 (dotted–dashed); cAM1, simultaneously stirred with NaOH (0.1 g/g) + water (0.1 g/g), located in different media: (*g*) I – air (dotted lines), II – $CDCl_3$ (dashed lines), and III – DMSO–d6 (solid lines), and (*h*) mixture of 3$CDCl_3$ + 1DMSO–d6; (*e*) WAW includes signals of OH^- (at $\delta_H < 0$ ppm) with a certain upfield shift; (*f*) signals: 1 is WAW, 2 $(CD_3)_2S{=}O\cdots H{-}O{-}H$, 4 – 5 SAW, and 6 water around Na^+

For hydro-compacted A–300, the summarized confined space and cryoscopic effects are stronger (Fig. 6 *a*) than those for loose initial A–300 (Fig. 5). These effects for A–300/H_3PO_4/water and cAM1/NAOH/DMSO/water are similar (Fig. 6) to those for initial A–300 (Fig. 5), but for cAM1/DMSO/water in chloroform–d, the effects are stronger (Fig. 6 *g*) because there are no competitive interactions of DMSO and NaOH (or acid) with water.

Maximal diminution of the Gibbs free energy of the bulk DMSO/water mixture is about –1.3 kJ/mol [20–23]. Maximal diminution of the Gibbs free energy of pure water bound to A–300 is about –3.0 kJ/mol [16]. In the case of complete additivity of CSE and CE, one could assume that $\Delta G_{CSE+CE} \approx -4.3$ kJ/mol. However, the experimental data give $\Delta G_{CSE+CE} \approx -3.5$ kJ/mol for a small fraction of the mixture located in the first adsorption layer at a surface of A–300 [16]. This could be considered as a partial additivity with reduced synergetic effect caused by both CSE and CE (in other words, CSE can partially inhibit CE). Similar results could be found for other solutions [16, 34–39]. This could be explained by the differences in the bulk and bound (confined) solutions because solvents located in pores or at a solid surface partially loss their activity and molecular mobility. One could assume that this loss could be stronger in narrower pores and for more concentrated solutions characterized by stronger CE in the bulk.

For TFAA/water bound to AM1 (Fig. 7 *e*,*f*), the CSE/CE influence is slightly greater than the CSE for water bound to AM1 in different dispersion media (Fig. 7 *a*–*d*). However, the size distributions of clusters and domains of unfrozen water and aqueous solutions demonstrate significant dependence on the kind of nanosilica (A–300 or AM1) and dispersion media (Fig. 8). This could be explained by several effects: (i) water is immiscible with chloroform but miscible with DMSO, but chloroform is miscible with DMSO; (ii) chloroform can displace water toward broader pores (voids between NP) to reduce the contact area between the immiscible liquids (this can lead to water freezing at higher temperatures than that in air) or toward narrower pores inaccessible for the $CDCl_3$ molecules larger than H_2O; (iii) any solvent activity decreases in pores; (iv) therefore, dissolution of water in DMSO and DMSO in water can be reduced with decreasing temperature upon location of unfrozen and concentrated solutions in narrower pores (voids); (v) ice is much pure than related aqueous solutions; (vi) therefore, concentrating of solutions occurs with decreasing temperature but CSE decreases the solubility degree that could lead partial phase separation. All these effects reflect in the PSD for pores infilled by unfrozen water or aqueous solutions (Fig. 8).

For hydrophilic A–300, intensity of the PSD for pores infilled by unfrozen water is slightly larger for A–300/water/air at small R values than that for A–300/water/chloroform, but there is the opposite effect for broad pores at $R > 15$ nm (Fig. 8 *a*). For the systems with AM1/water, the PSD intensity is much lower for the chloroform dispersion medium (Fig. 8) because of freezing of a great fraction of water (being practically unbound due to its displacement out of pores by chloroform) at T close to 273 K. This effect is absent for AM1/water/TFAA/chloroform due the cryoscopic and confined space effects; *i.e.*, a significant fraction of unfrozen water remains bound in pores (voids).

Appearance of tannic acid (with relatively large molecule $C_{76}H_{52}O_{46}$) in the interfacial layer at a surface of wetted hydrophilic (A–300) and hydrophobic (AM1) nanosilicas being in different dispersion media (air, $CDCl_3$ alone and with TFAA or HCl) leads to overlapping of the CSE and cryoscopic effect (Figs. 9 and 10). This overlapping does not result in the synergetic (CSE+CE) effects that is similar to other systems (Figs. 5–8) due to the reasons mentioned above (*i.e.*, CSE partially inhibits CE). However, it should be noted that the effects of HCl are stronger than those of TFAA or tannic acid. This could be explained by a smaller size of the Cl^- anions that allows the easy mixing of dissolved and dissociated acid molecules in narrower pores (voids) inaccessible for anions of TFAA and tannic acid, where the CSE are stronger. The theoretical calculations show (Fig. 9 *d*) that a small number of ions in the interfacial layer weakly affects the ^1H NMR spectra. This explains the absence of the acidic lines in the experimental spectra with decreasing solubility and dissociation degree of ion–generating solutes in the interfacial layers with decreasing temperature (Figs. 5–7 and 9). The meso/macroporosity of supra-NP structures of fumed oxides is confirmed by the size distributions of clusters of unfrozen water (Fig. 10 *b*, *c*) with a small contribution of unfrozen water and solutions located in narrow pores (voids) at $R < 1$ nm.

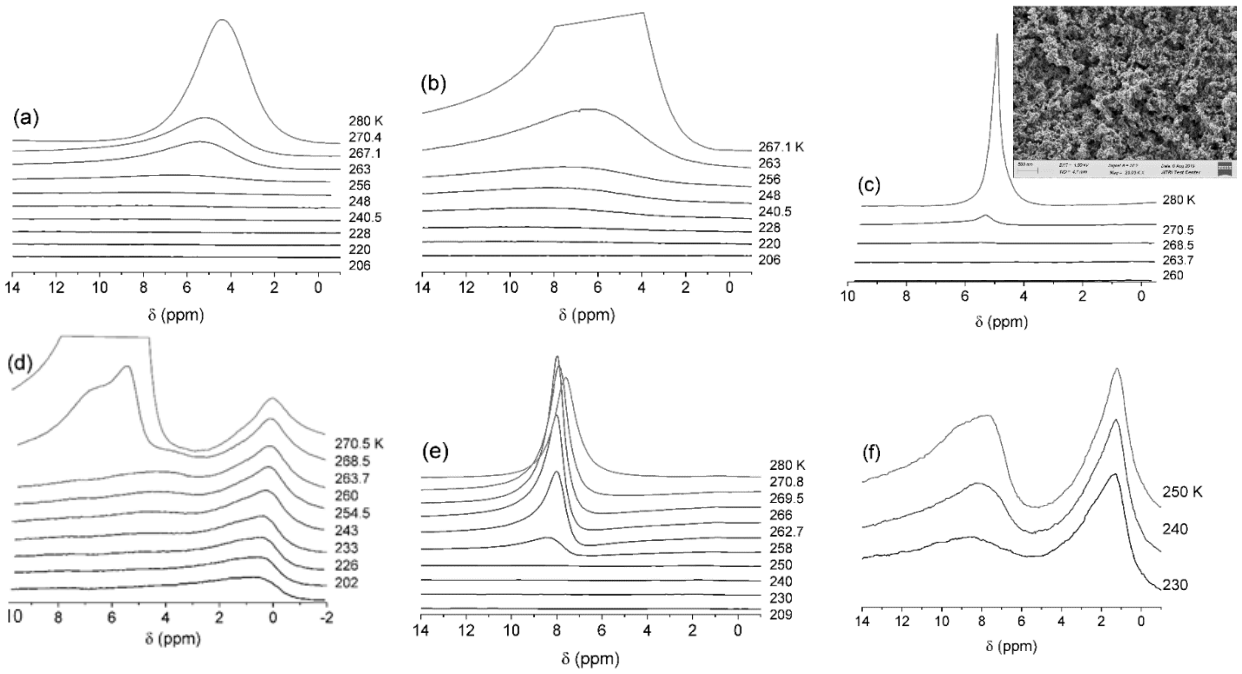

Fig. 7. ^{1}H NMR spectra of hydro–compacted AM1 (h = 1.4 g/g) located in different dispersion media: (*a*, *b*) air, (*c*, *d*) $CDCl_3$, and (*e*, *f*) $CDCl_3$/TFAA (4:1) (all spectra are shown in the left column, and the spectra at lower temperatures are shown in the right column) ((*c*) insert: SEM image of AM1, scale bar 500 nm)

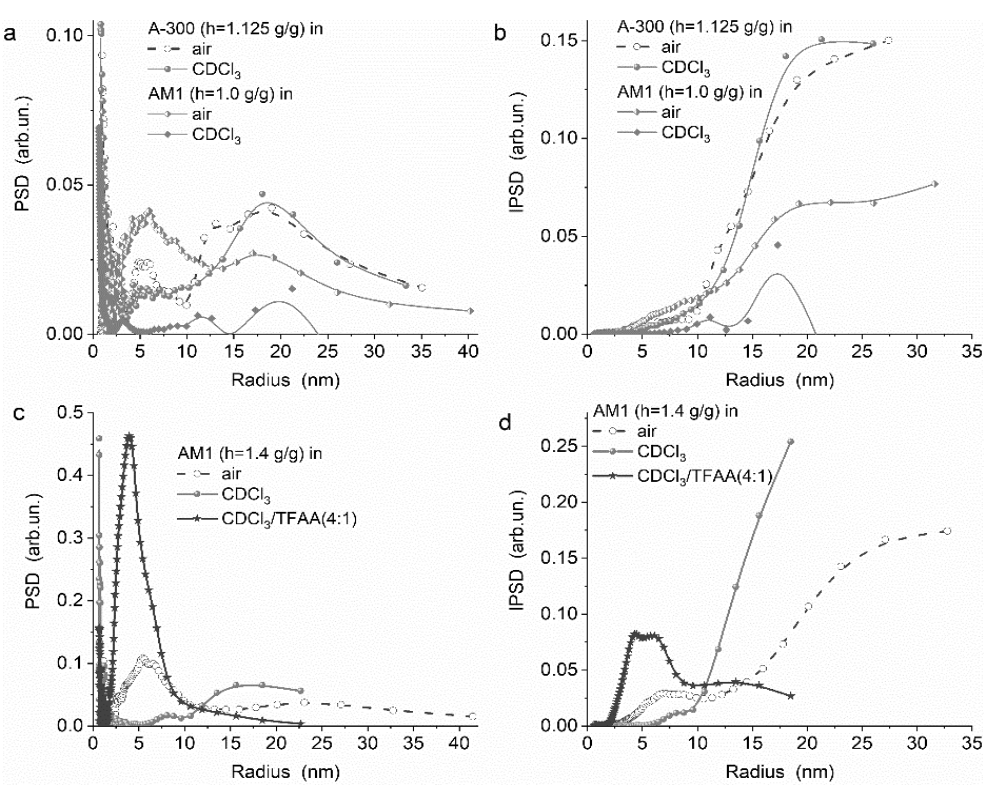

Fig. 8. NMR cryoporometry calculations of (*a*, *c*) differential and (*b*, *d*) incremental size distributions of pores filled by unfrozen water bound to hydro–compacted cAM1 at h = (*a*, *b*) 1 g/g and (*c*, *d*) 1.4 g/g and hydro-compacted cA–300 (*a*, *b*) at h =1.125 g/g located in air, $CDCl_3$ or $CDCl_3$/TFAA (4:1)

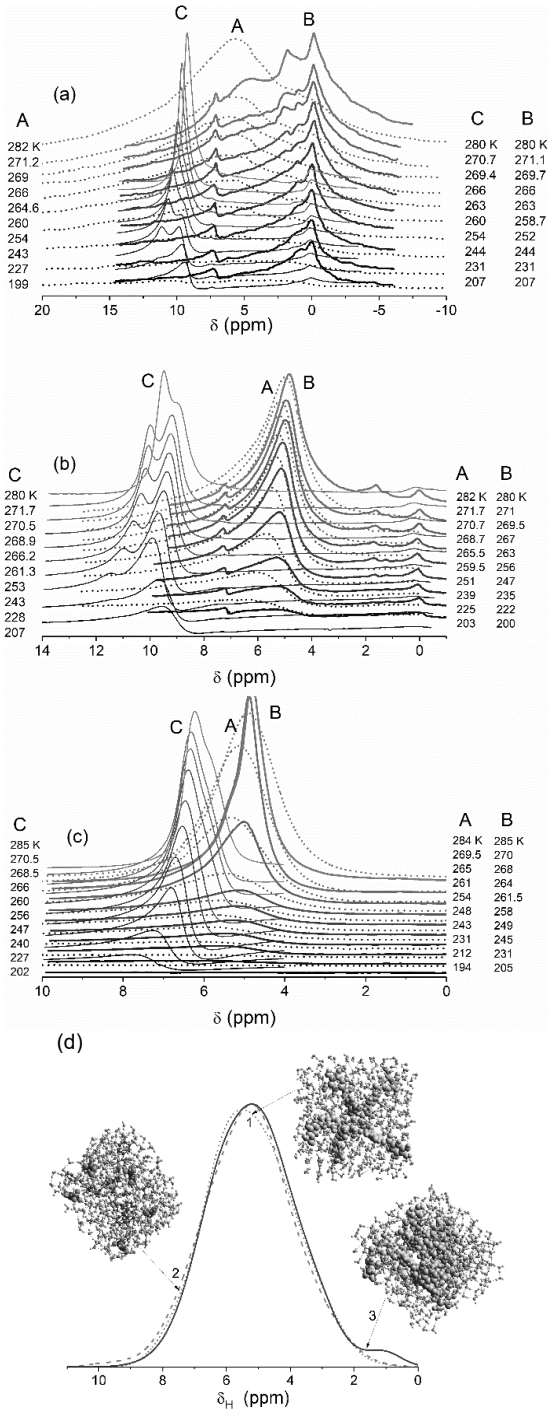

Fig. 9. ^{1}H NMR spectra of water bound to (*a*) AM1/tannin (1:1) at $h = 0.1$ g/g in air (spectra A), chloroform–d (B) and chloroform–d with TFAA (C) (6:1); (*b*) A–300/AM1 (1:1) with tannin (1:1) at h = 0.4 g/g in air (A), $CDCl_3$ (B) and $CDCl_3$/TFAA (C), (*c*) A–300/tannin (4:1) at $h = 0.4$ g/g in air (A), $CDCl_3$ (B), and in $CDCl_3$ with addition of 0.2 g/g of HCl/water (C); and (*d*) hydrated tannic acid $C_{76}H_{52}O_{46}$*$381H_2O$ (curve 1) and with addition of TFAA (six anions and six Zundel cations, curve 2), condensed two tannic acid molecules with $370H_2O$ (curve 3)

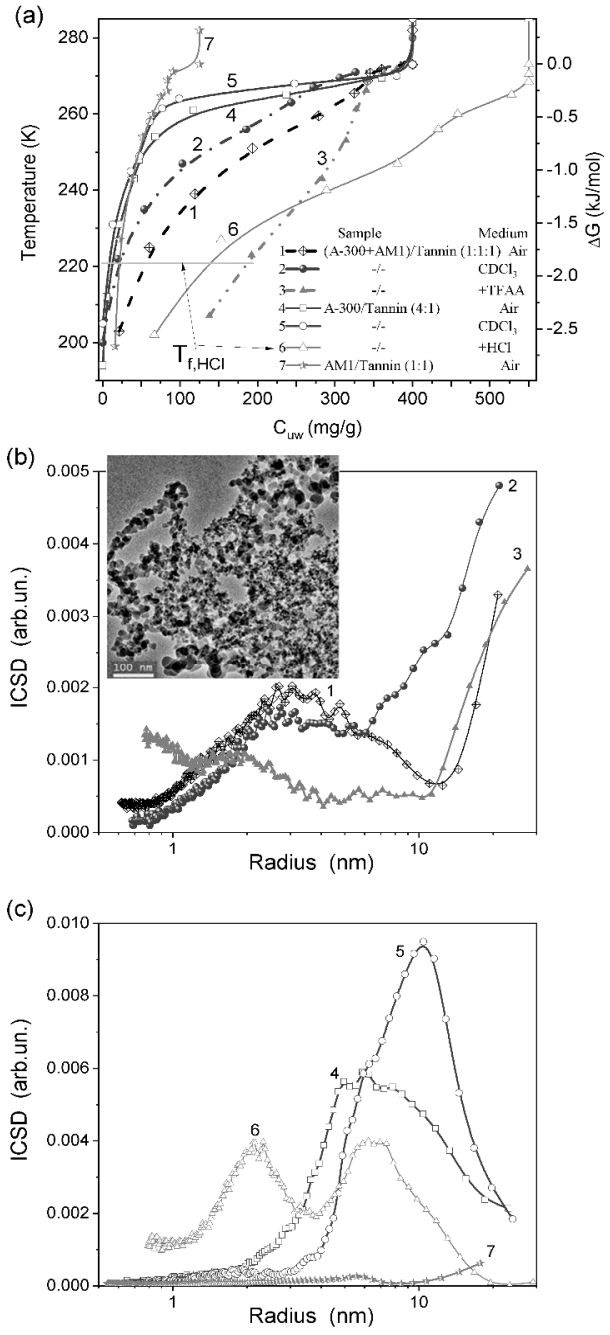

Fig. 10. (*a*) Temperature dependences of concentration of unfrozen water and changes in the Gibbs free energy *vs.* concentration of unfrozen water bound to A–300/AM1/tannin (1:1:1), A–300/tannin (4:1) and AM1/tannin (1:1) in different media (air, $CDCl_3$ and $CDCl_3$/acid), and (*b*, *c*) size distributions of clusters of unfrozen water (*b*) for samples 1–3 in (*a*) and (*c*) for samples 4–7 in (*a*) (*b* – insert: TEM image of AM1, scale bar 100 nm)

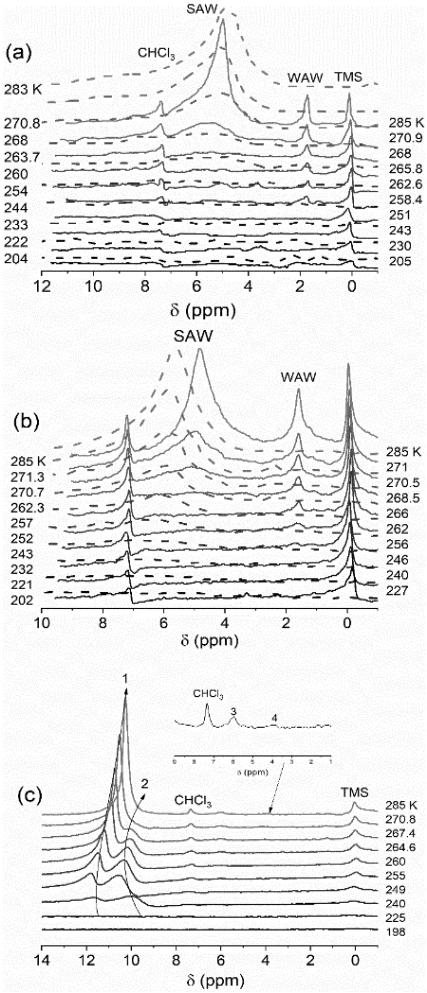

Fig. 11. ^{1}H NMR spectra of water (h = 0.5 g/g) bound to non–compacted (*a*) fumed alumina (Al–100) located in air (dashed lines) and chloroform (solid lines), and Al–100/AM1 (1:1) located in (*b*) air (dashed lines) or chloroform (solid lines), and (*c*) chloroform with addition of CF_3COOD (5:1)

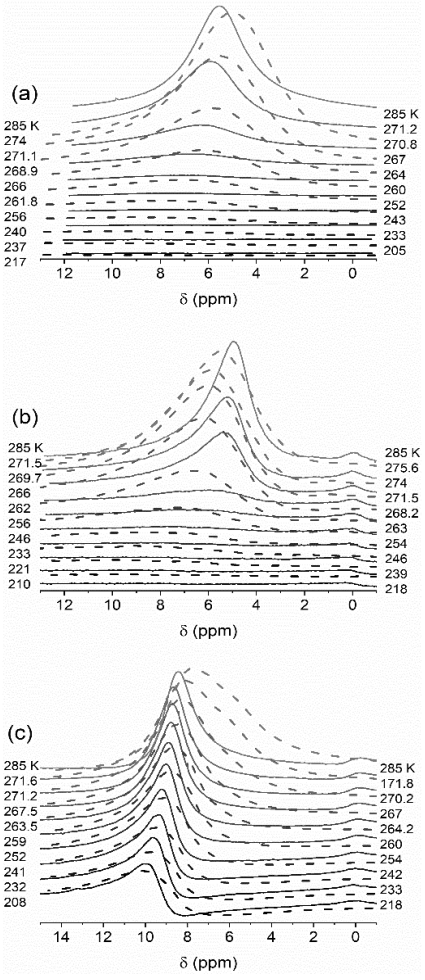

Fig. 12. ^{1}H NMR spectra of water (h = 0.5 g/g) bound to compacted (*a*) cAl–100 and (*b*) cAl–100/AM1 located in air (dashed lines) and chloroform (solid lines), (*c*) cAl–100 (dashed lines) and cAl–100/AM1 (solid lines) in $CDCl_3$ with addition of TFAA (5:1)

To study the influence of the surface structure on the interfacial and temperature behaviors of bound solutes, wetted fumed nanoalumina (label Al–100, S_{BET} = 89 m^2/g and V_p = 0.17 cm^3/g) alone or in the blends with AM1 was studied. In this case, the temperature behavior of bound water and aqueous solutions (Figs. 11 and 12) is similar to that for nanosilicas with respect to the CSE/CE. Thus, the confined space and cryscopic effects are stronger than the effects of a surface of weakly acidic A–300, hydrophobic AM1, or basic nanoalumina. Additionally, there are no the completely synergetic (CSE+CE) effects for these systems too. The absence of nanopores causes the displacement of bound water by chloroform toward broader voids (up to macropores, where a fraction of water becomes unbound), but addition of TFAA diminishes this effect (Fig. 13).

For hydro-compacted alumina/AM1 blend, the presence of hydrophobic silica affects the temperature behavior of bound water upon interaction with the chloroform dispersion medium (Figs. 13 and 14); *i.e.*, AM1 NP could provide screening of bound water (interacting with alumina surface) from the interaction with chloroform. Therefore, the main peak of the PSD for pores infilled by unfrozen water shifts toward smaller R values (Fig. 13 *b*) in comparison to non-compacted nanooxides (Fig. 13 *a*). Additionally, the extremal changes in the entropy of the

hydrogen bond network shift toward lower temperatures for compacted nanooxides (Fig. 14 *c*) in comparison to non-compacted ones (Fig. 14 *b*), and the region of these maxima is similar to that for $\lg T_2$ *vs* $1/T$ (Fig. 3). These results could be explained by certain enhancement of the CSE for compacted systems that leads to an increase in the FPD.

A weak CSE for OX–50 (Fig. 15) is due to its low textural characteristics (Table 1, Fig. 2 *d*). Additionally, a low content of H_3PO_4 causes a relatively weak CE (FPD is about of several degrees for the suspension and about –30 K for wetted OX–50/H_3PO_4 powders with respect to the related bulk solutions). Therefore, the summarized CSE + CE influence is less strong for the suspension (Fig. 15 *b*) than that for the wetted powders with greater $FPD_{CE,b}$ (Fig. 15 *a*). Thus, upon weak CSE (giving a small diminution in the solvent activity) and weak CE for the systems with low porosity, a clear synergetic (CSE+CE) effect could be observed (Fig. 15 *a*). However, even in this case, there is no complete additivity of both effects (since CSE inhibits CE).

A great CSE is characteristic for silica gel 200DF because it has only narrow pores, large SSA, and not small V_p (Table 1, Fig. 2 *a*). Therefore, the summarized CSE + CE are strong for any dispersion medium (Fig. 16), which can only weakly affect the behavior of liquids located in narrow pores. Note that the chloroform medium for 200DF/water/DMSO causes certain diminution of the summarized CSE/CE influence. This could be due to, at least, two effects: (i) displacement of the solution from pores (it is smaller one, since the amount of water is less than the V_p value and water can be located mainly in narrow pores poorly accessible for larger $CDCl_3$ and DMSO molecules), and (ii) dissolution of DMSO in chloroform (it is stronger one) that reduces the CE influence. The larger 'weight' of the second effect is confirmed by the effects caused by a diminution of the chloroform amount (Fig. 16 *b*) resulting in the stronger summarized CSE + CE influence (comp. with Fig. 16 *a*). However, there is no complete additivity of both effects as well as for other systems.

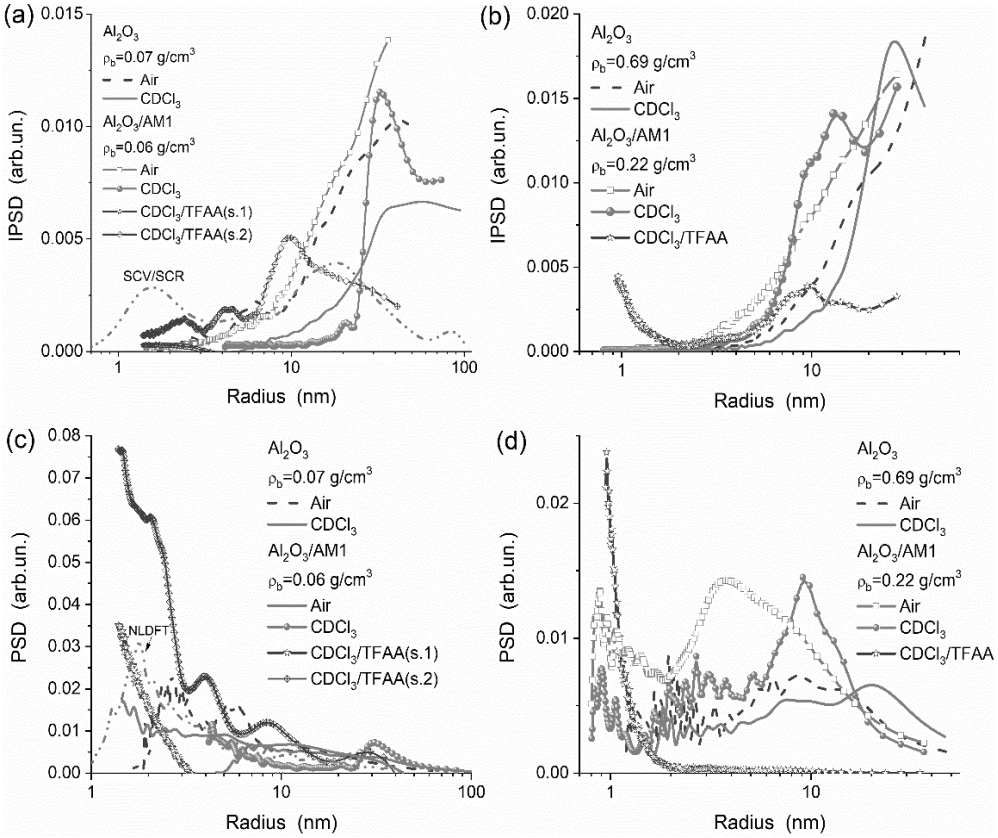

Fig. 13. (*a*, *b*) Incremental and (*c*, *d*) differential size distributions of unfrozen water clusters bound to (*a*, *c*) non-compacted and (*b*, *d*) hydro–compacted samples (PSD calculated from the nitrogen adsorption–desorption isotherms are shown for Al–100 in (*a*, SCV/SCR) and (*c*, NLDFT))

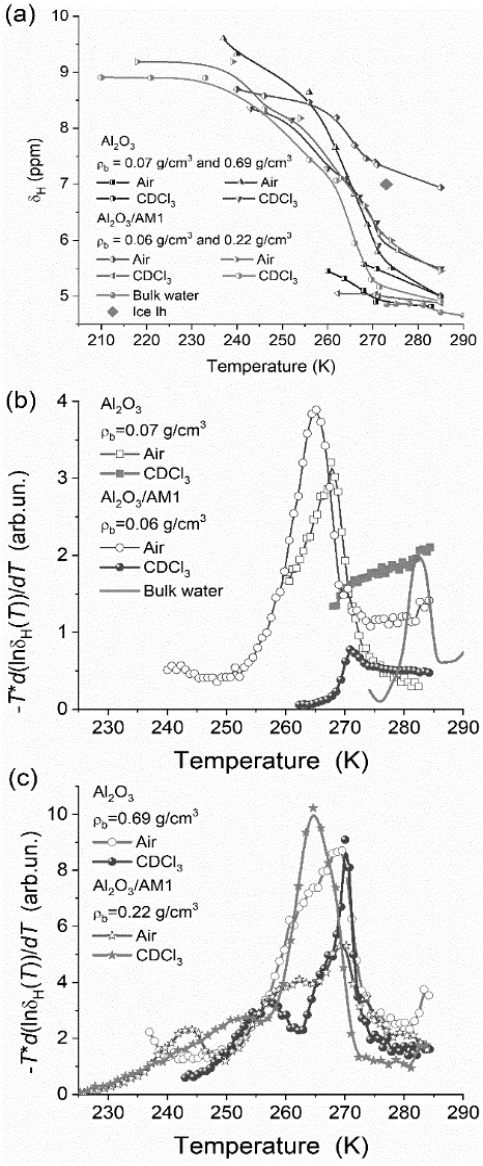

Fig. 14. (*a*) Chemical shifts of SAW in the ^{1}H NMR spectra of weakly hydrated (h = 0.5 g/g) non–compacted and compacted Al–100 and Al–100/AM1 located in air and chloroform alone, (*b*, *c*) function $-T(\partial(\ln\delta(T))/\partial T)_P$ *vs*. temperature for (*b*) non–compacted and (*c*) compacted Al–100 and Al–100/AM1 in air or $CDCl_3$

Note that the hydrophobicity of AM1, caused by the short DMS groups pair-crosslinked through the siloxane bonds, is not significant; therefore, a certain amount of water is adsorbed onto initial AM1 from air and remains after degassing [34, 39]. However, this amount is much smaller than that bound to hydrophilic nanosilica. The surface structure of AM1 with DMS provides enhanced clusterization of water bound to AM1 in comparison to A–300. This effect leads to the appearance of weakly associated water, which is maximum 1D/2D clustered with disordered HBN and characterized by low values of δ_H = 0.5–1.5 ppm. WAW is observed in the ^{1}H NMR spectra of cAM1/water and cAM1/NaOH/water in contrast to similar systems based on cA–300 and observed without WAW [34]. Strongly associated water characterized by $\delta_H \geq 3$ ppm is less clustered (in larger domains with more ordered HBN similar to that in the bulk water) than WAW, and it is observed in the systems studied (Fig. 17). Polar solutes, especially ion-forming electrolytes such as NaOH, can strongly affect the HBN and δ_H values. Solvated cations provide the downfield shifts for neighboring water molecules (due to decreased electron density around protons). The

anions OH^- characterized by the opposite upfield shifts (due to increased electron density around protons) can polarize water molecules and change their organization in the clusters and domains (that can lead to the downfield shift).

These effects depend also on the chaotropic and kosmotropic properties of solutes and co-solvents, since the HBN disordering leads to a diminution of the δ_H values. Note that the Na^+ ions are weakly kosmotropic in contrast to H^+ (strongly antichaotropic). Weakly polar chloroform is chaotropic (without the formation of strong HB with water molecules). Polar DMSO is weakly kosmotropic (it forms strong HB with water molecules but generates some disorder in the water organization due the CD_3 groups), as well as OH^- [19, 30]. Additionally, hydrophilic surface functionalities of A–300 could be assigned to kosmotropic ones in contrast to chaotropic DMS groups at the AM1 surface. The latter could provide the upfield shifts for strongly clustered water that are well observed as WAW (Fig. 17). As a whole, the summarized CSE+CE influence on the temperature behavior of the solutions bound to AM1 is similar to that for hydrophilic nanosilica A–300 (*i.e.*, there is CSE inhibition of CE).

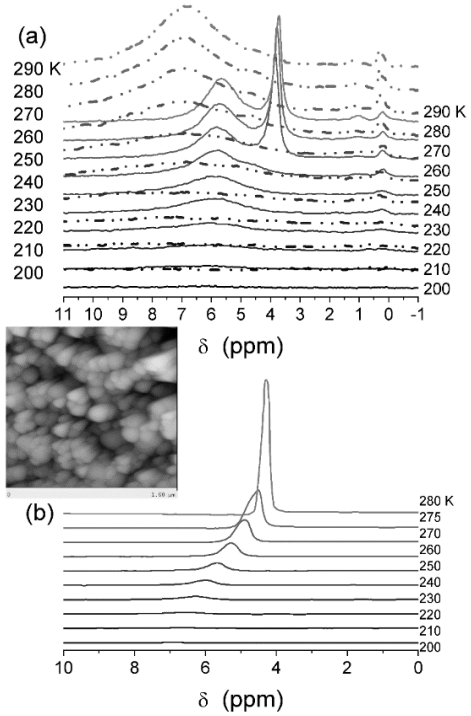

Fig. 15. ^{1}H NMR spectra recorded at different temperatures of dried OX–50/H_3PO_4 powder at h = (*a*) 25 (solid lines) and 45 mg/g (dotted–dashed lines) in CCl_4 medium and (*b*) frozen aqueous suspension with OX–50 (16 wt. %) and H_3PO_4 (4 wt. %) (insert: AFM image of OX–50, 1 μm×1 μm)

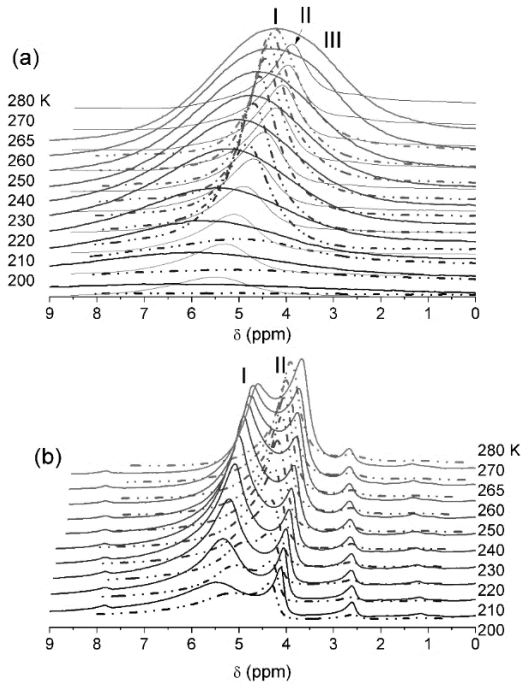

Fig. 16. ^{1}H NMR spectra of water (h = 0.18 g/g) bound to silica gel 200DF (S_{BET} = 540 m^2/g, V_p = 0.34 cm^3/g) in $CDCl_3$ (a, I, $\Delta T_{CSE} \approx -70$ K) and with the presence of DMSO–d_6 in (a, II, 1 g/g, $\Delta T_{CE,b} \approx -10$ K) air or $CDCl_3$ (a, III, 0.1 g/g ($\Delta T_{CE,b} \approx -20$ K), b, 1 g/g, $\Delta T_{CE,b} \approx -10$ K); $CDCl_3$ amount (*a*) 4.5 g/g and (*b*) I, 3 g/g and II, 1.5 g/g

The HBN disordering effect is enhanced in the chaotropic $CDCl_3$ medium giving a cooperative effect with the DMS groups at the AM1 surface. The mixtures of $CDCl_3$ with DMSO may provide complex effects on water bound to A–300 and AM1 depending on the volume ratio of co-solvents. There is an important factor affecting changes in the interfacial and temperature behaviors of liquids (solvents with solutes) in pores (voids in supra-NPNP structures), because in pores or thin surface layers at NPNP, any solvent loses its characteristic properties (*e.g.*, kosmotropic or chaotropic) and becomes rather a poor solvent, and bound solutes can segregate to form nearly pure own phase. Clearly, this inhibits possible synergetic CSE+CE influence on the bound solution.

The aqueous solution of NaOH (at pH > 10) is aggressive with respect to a silica surface.

Therefore, a low amount of water is used in this study to prevent negative intensive processes of the dissolution of a surface of both A–300 and AM1 (note that the mentioned negative effect is diminished at low temperatures used). Thus, there are several various and sometimes opposite factors affecting the interfacial and temperature behaviors of water and NaOH/water bound to hydrophobic and hydrophilic silicas. To analyze these factors, one could fix low amounts of NaOH and water in all the systems and vary solids (A–300 and AM1), dispersion media (air, $CDCl_3$, DMSO-d6 and their mixtures), and observation temperature because the interfacial behavior of SBW, WBW, SAW, and WAW, as well as solutes, is a function of temperature and surroundings.

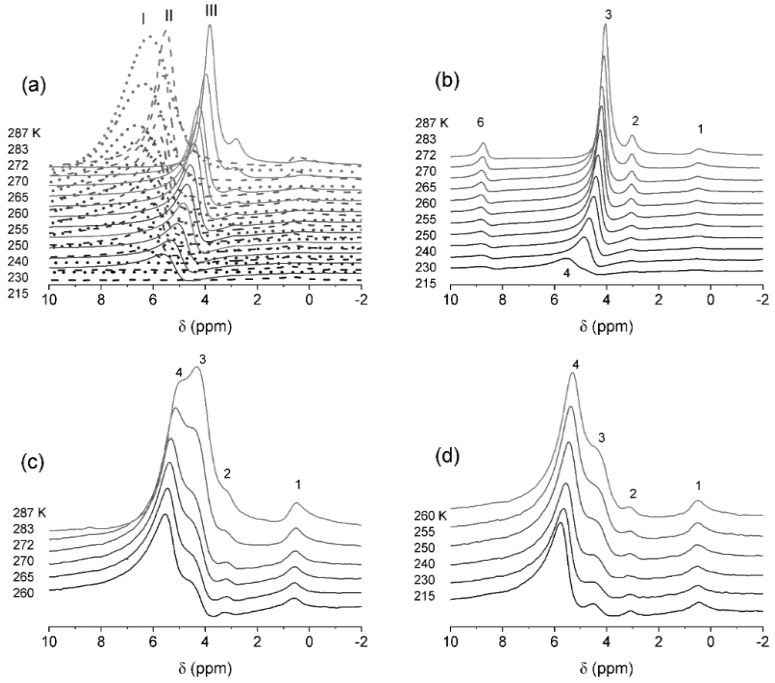

Fig. 17. ^{1}H NMR spectra of cAM1 subsequently stirred with NaOH (0.1 g/g) and then with water (0.1 g/g) and located in different media: (*a*) I – air (dotted lines), II – $CDCl_3$ (dashed lines), and III – DMSO–d6 (solid lines), (*b*) mixture of 1$CDCl_3$ + 3DMSO–d6, and (*c*, *d*) mixture of 3$CDCl_3$ + 1DMSO–d6 (in different temperature ranges)

The effect of step-by-step melting of bound frozen adsorbates leads to increasing intensity of signals, especially SAW, with increasing temperature. This allows one to estimate the amounts of unfrozen water in various structures (SAW, WAW, SBW, and WBW) *vs*. temperature. The weakening solvent effect in pores is confirmed by relatively low signal at 3 ppm (in comparison to SAW signal at $\delta_H > 4$ ppm) related to the HB $(CD_3)_2S{=}O\cdots H{-}O{-}H$ for water dissolved in DMSO for all the systems located in DMSO alone or in mixtures with $CDCl_3$ (Fig. 17) [34]. Thus, despite water and DMSO are well miscible in the bulk, their mixing in pores (voids) is restricted. This effect could be enhanced by stronger interactions of water with NaOH, which cannot be dissolved in $CDCl_3$ and DMSO but could be partially dissolved in SAW with increasing temperature, than with DMSO.

For complex $CDCl_3$/DMSO-d6 dispersion media, the spectral pictures depend on the stirring type (subsequent addition of NaOH and water or simultaneous one) and $CDCl_3$/DMSO-d6 volume ratio, as well as on temperature (Fig. 17). There are, at least, six signals of the protons in water with different surroundings. The first one at $\delta_H \approx 0.5$–1.0 ppm is due to WAW appearing at the surface of AM1 (*e.g.*, between the DMS groups) under the cooperative chaotropic DMS and $CDCl_3$ effects. The second one at $\delta_H \approx 3$ ppm is due to the $(CD_3)_2S{=}O\cdots H{-}O{-}H$ complexes of water dissolved in DMSO. The third one at $\delta_H \approx 3.5$–5.5 ppm is due to SAW without or with DMSO molecules dissolved in a small amount (SAW could split, Fig. 17 *c*, *d*). The next signal 4 could be attributed to SAW interacting with non-ionized clustered NaOH. The fifth signal corresponds to SAW with small amounts of dissolved NaOH and DMSO. The sixth

signal is due to SAW with dissolved and spatially separated ions Na^+ and OH^-. Note that the WAW clusters (as well as $CDCl_3$ and DMSO) cannot dissolve NaOH.

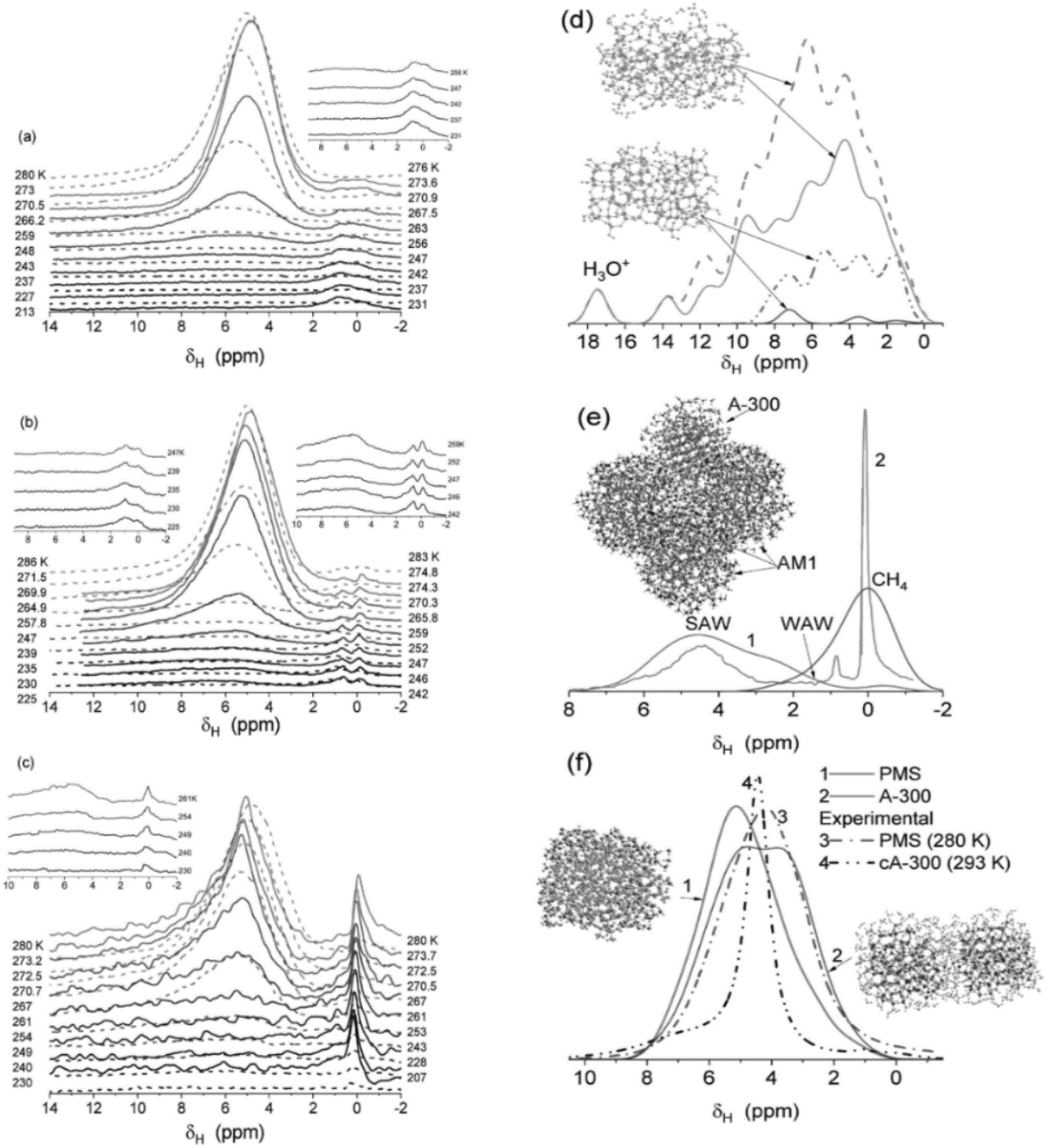

Fig. 18. ^{1}H NMR spectra of bound water and methane recorded at different temperatures for AM1 and AM1/A–300 (b, solid lines and right insert) at h = (*a*, *b*) 1 g/g and (*c*) 0.33 g/g (solid lines) and 0.66 g/g (dashed lines) for samples without (a, dashed lines, c) and with (a, solid lines, b) treatments with liquid nitrogen (77.4 K); theoretical spectra of water and surface functionalities: (*d*) silica cluster with 88 units and 64 H_2O (upper curves) and $10H_2O$ (bottom curves) for water and silanols (dotted-dashed lines) and only bound water (solid lines) (GIAO/ωB97X–D/cc–pVDZ); (*e*) AM1/A–300 (3:1) model with bound $608H_2O$+$66CH_4$ (PM7) (curve 1) and experimental spectrum of AM1/A–300 (3:1) at h = 0.1 g/g and 285 K (curve 2); and (*f*) theoretical spectra of water bound to PMS (curve 1) and two silica particles (curve 2) and experimental spectra of wetted PMS (curve 3) and cA–300 (curve 4)

For subsequently stirred cAM1 with NaOH and then with water, SAW bound in the systems located in individual dispersion media demonstrates features (Fig. 17 *a*) similar to that for the simultaneously treated systems. However, for the former, the WAW signal intensity is lower due to better interaction of water with NaOH. For the $CDCl_3$/DMSO-d6 mixtures (Fig. 17), the spectral picture depends also on the co–solvents volume ratio. For $CDCl_3$/DMSO = 3/1 v/v, only signals 1–4 are observed (Fig. 17 *c*, *d*). Intensity of signals 3 and 4 depends differently on temperature. Freezing-out of water responsible for signal 3 is more intensive (due to a larger contribution of WBW in this SAW) than that of water related to signal 4 (larger contribution of SBW in SAW). The proton and water-molecular exchange processes between the water clusters related to signals 3 and 4 are slow (in the NMR time scale) since $CDCl_3$ (of a larger amount) can form barriers between the spatially separated water clusters. For $CDCl_3$/DMSO = 1/3 v/v, the exchange is faster, since DMSO (producing weak barriers for water diffusion) can dissolve water much stronger than $CDCl_3$, signals 3 and 4 join and split only at 215 K (Fig. 17 *b*). Additionally, signal 6 for water interacting with dissociated NaOH is also observed [34].

Upon methane adsorption onto wetted AM1 (h = 1 g/g, ρ_b = 0.5 g/cm^3), only signal of strongly associated water (δ_H = 5–7 ppm) is observed in the ^{1}H NMR spectra of static sample at 213–280 K (Fig. 18 *a*, dashed lines). Intensity of water signal decreases with lowering temperature due to partial freezing-out of bound water. The water amount is twice larger than the pore volume (mesopores + macropores) of initial AM1 powder degassed (Table 1, V_p). Therefore, water can infill nanopores and mesopores that prevents the adsorption of methane. The water adsorption onto AM1 as a hydrophobic nanosilica could be clustered and form larger domain with increasing water content (Fig. 18 *d–f*, models). However, the water amount at h = 1 g/g is too large to form small clusters with empty voids between them and NP accessible for methane molecules.

Nonpolar or weakly polar organic liquids (immiscible with water) can displace adsorbed water from pores (voids) of hydrophilic and hydrophobic adsorbents to reduce contact area between immiscible liquids [16]. At standard pressure, melting and boiling points of methane are 90.7 K and 111.7 K, respectively. Thus, bulk methane at 77.4 K (liquid nitrogen) is solid, but it could be in quasi-liquid state in narrow voids according to the Gibbs–Thomson relation for the freezing point depression for liquids confined in pores. This quasi-liquid methane can affect the organization of NPNP in secondary structures as well bound water forming ice upon fast precooling at 77.4 K. At 77.4 K water transformed into ice clusters having larger volume than liquid water and characterized by different size distribution than water clusters have. Fast precooling (77.4 K) of wetted various adsorbents can result in significant changes in the sample porosity. To check the effects of precooling and adsorbed methane on the organization of wetted AM1 powder, the latter was fast frozen (77.4 K) in NMR ampoule with attached vessel with methane (excess pressure 1.1 bar, room temperature) for 1 h. Then this ampoule was placed into NMR device being at 230 K and equilibrated at each increased temperature (Fig. 18 *a*, solid lines, insert). The measurements were repeated (second precooling at 77.4 K, then equilibration at 225 K, and heating to 286 K) for this sample (Fig. 18 *b*, dashed lines, left insert). The treatments result in a significant increase in the adsorbed methane amounts in comparison to AM1 (h = 1 g/g) without precooling, but it slightly decreased after the second precooling in comparison to the first one. Methane gives ^{1}H NMR signals around 0 ppm with intensity depending more weakly on temperature than that of bound water because the spectra were recorded at temperatures higher than the boiling point of methane $T > T_{b,CH4}$ and lower than the melting point of bulk ice $T < T_{m,H2O}$. Bound methane signals change due to its adsorption-desorption, but water signals change due to freezing-melting of bound water/ice.

The presence of two signals of bound methane can be due to the adsorption in narrower and broader voids in the nanopores (R < 1 nm) and narrow mesopores (R = 1–2 nm) ranges. The latter are observed for dry degassed nanosilicas. However, nanopores mainly absent in degassed silicas could be due to secondary porosity caused by ice nanoclusters located in mesovoids in treated supra-NPNP structures. Location of methane molecules in various voids with different structure of pore walls (siloxane bridges, silanols, dimethylsilyl groups, water/ice clusters) leads to the difference in local magnetic anisotropy that

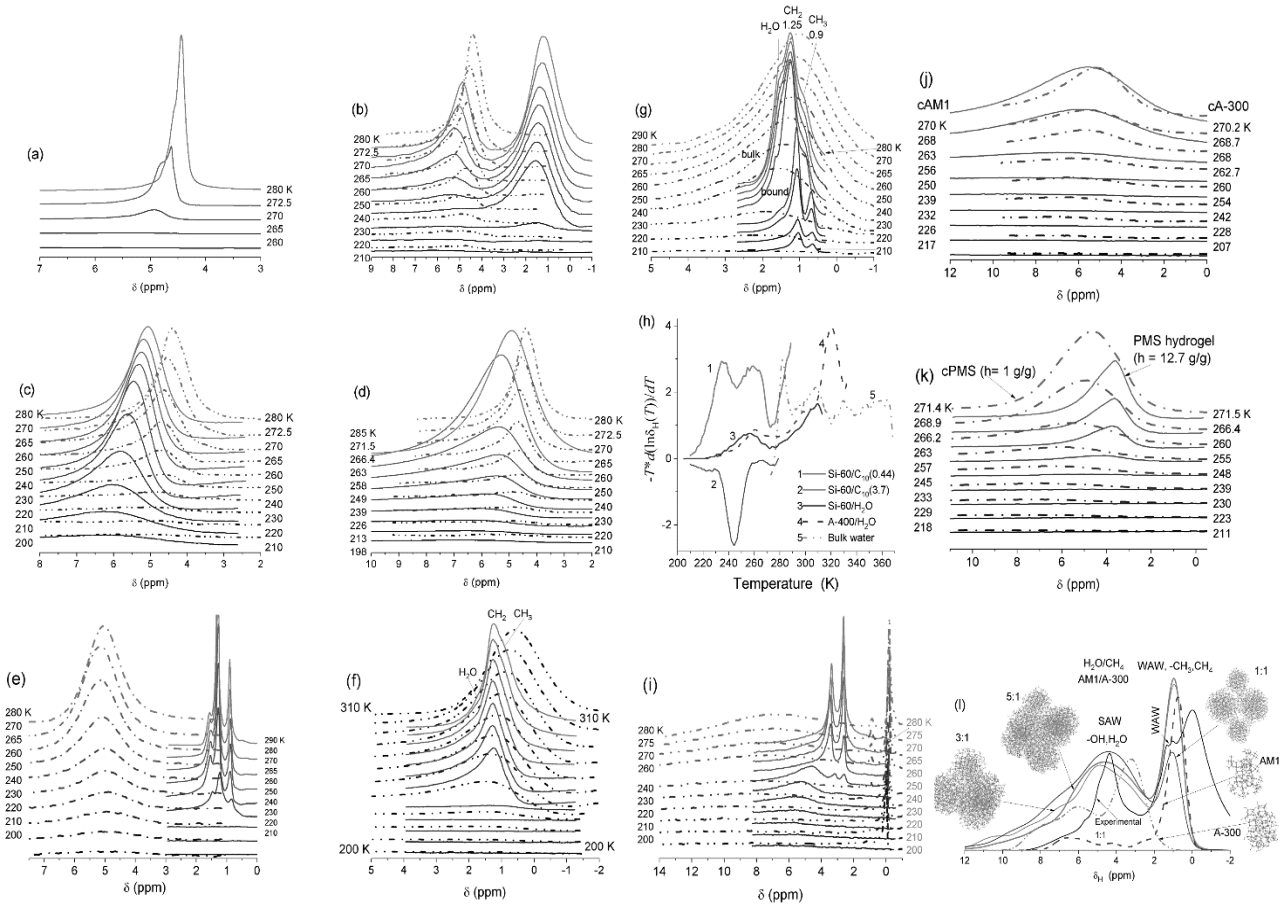

Fig. 19. ^{1}H NMR spectra of water bound to (*a*–*d*) Syloid® 244 and (*c*) cA–300 (wet MCA for 6 hours) at water content h = (*a*) 0.9 g/g, (b) 0.3 g/g and with decane (0.7 g/g), (*c*) 0.1 g/g (cA–300) and 0.3 g/g (Syloid), (*d*) Syloid at h = 0.3 g/g and silica gel Si–100 at h = 0.5 g/g; hydrophilic nanosilica (S_{BET} = 409 m^2/g) (*e*) initial (ρ_b = 0.07 g/cm^3) and (*f*) compacted (ρ_b = 0.15 g/cm^3): (*e*) water (h = 0.02 g per gram of silica, dotted–dashed lines); and water (h = 0.05 g/g) and *n*–decane of content C_d = 7.3 g/g (solid lines), (*f*) with polyphosphoric acid (PPA) at C_{PPA} = 0.73 g/g (dotted–dashed) and 3.7 g/g (solid lines); (*g*) sorbates bound to Si–60 at decane amount C_d=0.44 g/g (dotted–dashed) and 3.7 g/g (solid lines) and residual water at $h \approx 0.005$ g/g.; (*h*) function $-T(\partial \ln\delta(T)/\partial T)_P$ *vs*. temperature for *n*-decane (C_{10}) and water bound to Si–60 or A–400; (*i*) water at h = 0.17 g/g and methane bound to single-layer graphene oxide, SLGO (dotted–dashed) and water interacting with SLGO in CCl_4/DMSO–d_6 (1.5/1) medium (solid lines); (*j*) cAM1 at h = 1 g/g (solid lines) and cA–300 at h = 1.125 g/g (dotted–dashed) in air; (*k*) initial hydrogel PMS (solid lines) and wetted dry PMS then hydro–compacted (cPMS, dotted–dashed lines); and (*l*) theoretical ^{1}H NMR spectra of water, methane, and surface functionalities for models of AM1 and A–300 blends (PM7 method); clusters of dry AM1 (dashed line) and weakly hydrated A–300 (dotted–dashed) alone (GIAO/ωB97X–D/cc–pVDZ); and experimental spectrum of water and methane bound to AM1/A–300 (1:1)

results in the appearance of two signals or poorly split, broadened signal (Fig. 18). The methane signal splitting or broadening is observed for all samples at different hydration, but this effect is stronger after sample precooling by liquid nitrogen. Water bound to AM1/A–300 (precooled at 77.4 K) is frozen at lower temperatures than water bound to AM1 alone (Fig. 18) because A–300 is hydrophilic and can form a larger number of stronger hydrogen bonds with water molecules than hydrophobic AM1 can do. A certain amount of residual silanols remaining in AM1 (steric effects prevent complete crosslinking of silanols upon the nanosilica reaction with dimethyldichlorosilane hydrolyzed) cannot provide the same structure of a water adsorption layer as for A–300.

Co-sorbates, dispersion media, solute, colligative properties, and CSE could be cooperative or opposite depending on various factors such as amounts of co-sorbates and solutes, textural and structural characteristics of sorbents, their hydrophilicity and hydrophobicity, surface nonuniformity, temperature, *etc*. (Fig. 19). At a low content of sorbates, they locate in the narrowest pores where CSE and FPD are maximal, molecular mobility is low (observed using NMR, differential scanning calorimetry (DSC) at $T < T_{m,f}$ and thermogravimetry (TG) evaporation at $T > T_{m,f}$) [16]. For hydrophilic sorbents, these effects lead to downfield shifts of ^{1}H NMR signals becoming broader (due to decreased molecular mobility and restrictions in proton-exchange reactions). For carbon materials, there is additional effect due to strongly increased magnetic shielding of the protons by π–electron clouds at basal carbon planes that is stronger in narrower pores with more ordered wall structure (similar to graphite). Enhanced amorphism and functionalization of carbon surfaces result in diminution of upfield shifts, which are smaller for sorbates bound to graphene oxides than AC (Fig. 19).

Decane excess (3.7 g/g, V = 5.07 cm^3/g) located out of pores of Si–60 (V_p = 0.753 cm^3/g) results in more strongly decreased entropy at $T_{m,f}$ than at 0.44 g/g (Fig. 19 *h*). For the latter, there are two entropy peaks due to melting process in pores of different sizes. Changes in the entropy of bound water could have several extrema (Fig. 19 *h*) due to freezing/melting of water/ice at different temperatures in pores of different sizes because of the CSE+CE influence. These results show interfacial phenomena complexity *vs*. temperature and pore sizes that are also affected by sorbate/sorbent kinds.

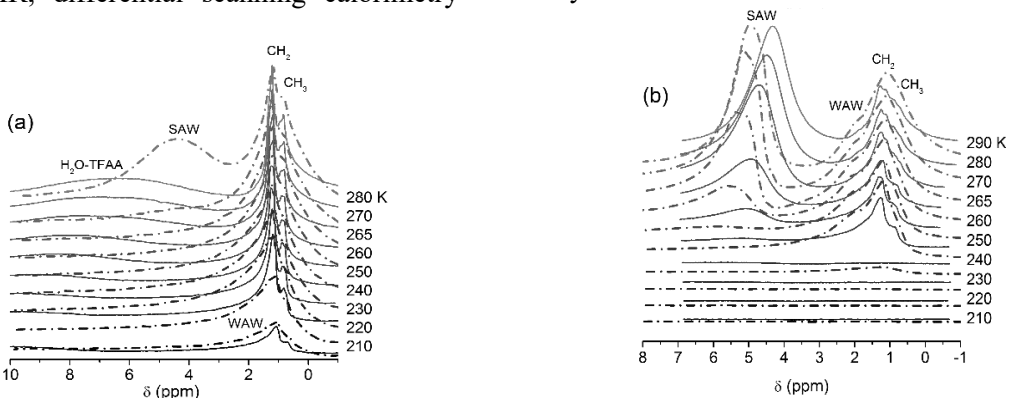

Fig. 20. ^{1}H NMR spectra recorded at different temperatures of water and *n*-decane bound to the NaCl powder in (*a*) $CDCl_3$ (dash–dotted lines) and $CDCl_3$/TFAA (9:1) (solid lines) at 0.1 g/g of water and 0.1 g/g of decane; (*b*) a mixture of hydrated PMS (h = 9 g/g) with decane (1 : 1) (dash–dotted lines) and a mixture with hydrated PMS/KCl (1 : 3) at h = 9 g/g and decane (4 : 1) (solid lines)

Water bound to NaCl with the presence of *n*-decane (miscible with chloroform and immiscible with water, *i.e*., water + decane – no CE, but NaCl or TFAA + water or decane + chloroform – there is CE) shows a broad signal at $\delta_H \approx 4.5$ ppm at 280 K (Fig. 20 *a*, dash-dotted lines). At 270 K, its intensity becomes much lower and it disappears at 265 K due to freezing of water. This suggests that all water is weakly bound, because it is frozen close to the freezing point of bulk water. This water is strongly associated since δ_H is close to that of bulk water. Decane gives two signals at δ_H = 0.95 ppm (CH_3 groups) and 1.25 ppm (CH_2) (Fig. 20 *a*). At low

temperatures, a weak signal at 1.5–2.0 ppm can be assigned to WAW. Addition of a certain amount of TFAA to chloroform (1:9) leads to a downfield shift of signal of TFAA/water toward 7–8 ppm. It is broad at high temperatures and shifts toward 10 ppm with decreasing temperature close to that for bulk TFAA solution (~11 ppm). Thus, the summarized CSE+CE (with certain synergism) are observed for both water and decane even at 200 K at the presence of TFAA, but NaCl does give the similar effect (Fig. 20 *a*).

A decrease in the content of decane and addition of KCl to hydrated PMS result in unexpected upfield shift of water signal from 5–6 ppm (dash-dotted lines) toward 4.5–5.0 ppm (solid lines, Fig. 20 *b*). This result can be explained by diminution of sizes of bound water structures after addition of KCl. In contrast to the systems with NaCl (Fig. 20 *a*), signals of water and decane are not observed at $T < T_{f,d} = 243.5$ K (freezing point of bulk *n*-decane) (Fig. 20 *b*). However, in the presence of KCl signal of water is observed at 250–260 K. Thus, a small fraction of SAW is strongly bound, and signal of WAW disappears at low temperatures even at $T < T_{f,d}$. Certain broadening of decane signal can be due to nonuniformity of magnetic susceptibility of samples including relatively large solid particles of salts. The CSE+CE influence for the PMS/KCl/water/chloroform is weaker than that for NaCl/water/chloroform without or with TFAA. This could be explained by the PMS effect enhancing the phase separation with lowering temperature. Therefore, decane is frozen at $T < T_{f,d} = 243.5$ K (Fig. 20 *b*). This is confirmed by the results for similar systems with hydrophilic A–300 (Fig. 21).

In a mixture of hydrophilic A–300 nanoparticles with small KCl particles being in air, the freezing point depression is observed for both bound water and decane (Fig. 21 *a*). Unfrozen water is observed even at 210 K and decane at 220 K. Water forms relatively small structures in narrow voids between silica and salt particles. In $CDCl_3$ medium, lines become narrower (due to diminution of molecular exchange effects) (Fig. 21 *b*). A portion of water is displaced from pores. This leads to differentiation of signals, since two signals of SAW are observed at $\delta_H = 5$ ppm (SAW1) and 3.5 ppm (SAW2), as well as WAW at $\delta_H = 1.7$–2.0 ppm. Addition of CD_3CN to this mixture (Fig. 21 *c*) causes the upfield shift of water signals and a relative increase in the amounts of SAW2 and a decrease in the content of SAW1. This suggests decreasing associativity of bound water molecules. Addition of TFAA (Fig. 21 *d*) results in simplification and averaging of the spectra due to fast proton exchange between molecules of water and TFAA. Intensive signal of the aqueous solution of TFAA is observed at 10 ppm. Replace of NaCl by KCl (Fig. 21 *e*) or LiCl (Fig. 21 *f*) leads to enhancement of SAW1, including both SBW and WBW. Appearance of these waters corresponds to the formation of relatively small structures since SAW2 is rather closer to WAW than to SAW1.

The maximal difference in changes in the Gibbs free energy of solvation of non-dissociated is for LiCl. Calculations with SMD/B3LYP/6–31G(d,p) clusters $M_{10}Cl_{10}$ (M = Li, Na) and K_8Cl_8 with the geometry optimized using the HF/6–31G(d,p) method give for solvation in water and *n*–decane, respectively: –41.3 and –34.9 kJ/mol ($Li_{10}Cl_{10}$), –28.2 and –24.9 kJ/mol ($Na_{10}Cl_{10}$), and –22.5 and –18.2 kJ/mol (K_8Cl_8).

Thus, the difference for KCl particles in solvation by water and decane adds a reason to form of large decane structures (weakly bound to PMS/KCl) with the properties close to that of bulk decane. A significant decrease in the amounts of water from $h = 9$ g/g bound to PMS to 0.1–0.15 g/g bound to silica with salts or individual NaCl leads to enhancement of the interfacial effects on decane. In many cases, the freezing point depression effects are stronger (possible partial synergetic CE for salt solutions) than the melting delay effects. Both effects depend more strongly on the textural characteristics and the amounts of water (*i.e.*, infilling of pores by water) than the types of silica and salts. The latter can be explained by relatively weak effects of salt crystallites or dissolved ions on the ^{1}H NMR spectra of water without of adsorbents or bound to silica because all the spectra are characterized by a signal at 4–5 ppm typically observed for bound SAW (Figs. 20 and 21) or bulk water. The spectrum of hydrated LiCl nanoparticles is slightly different due to partial dissolution of LiCl and formation of charged particles including H_3O^+ and OH^-. Anions Cl^- are chaotropes but cations Li^+ are kosmotropes, which differently affects the water structure, especially at a surface of polar nanoparticles.

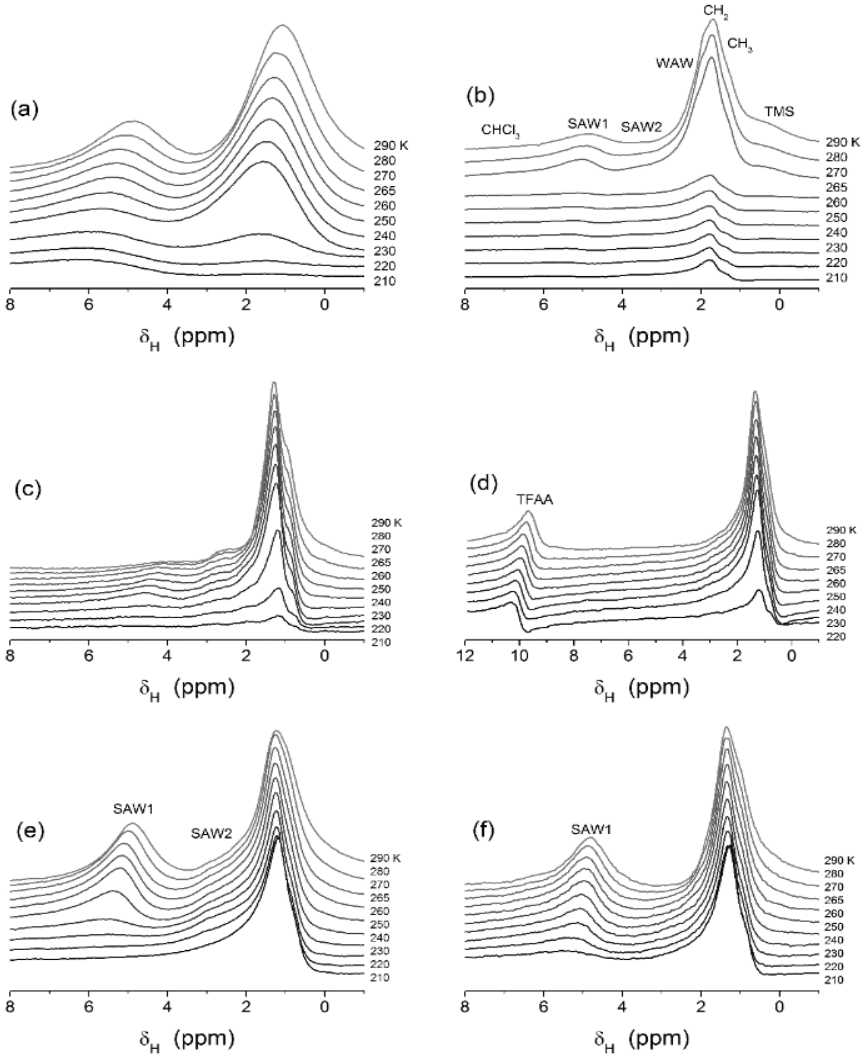

Fig. 21. ^{1}H NMR spectra recorded at different temperatures of water and *n*–decane bound to (*a*) A–300/KCl (6 : 1) at h = 0.1 g/g and C_d = 0.2 g/g in air; (*b*) A–300/KCl (6 : 1) at h = 0.1 g/g in a mixture with $CDCl_3/C_{10}H_{22}$ (7 : 1); (*c*) A–300/NaCl (6 : 1) at h = 0.1 g/g and C_d = 0.15 g/g in a mixture $CDCl_3/CD_3CN$ (4:1) medium; (*d*) A–300/NaCl (6 : 1) at h = 0.1 g/g and C_d = 0.15 g/g in a mixture $CDCl_3/CD_3CN$/TFAA (4:1:1) medium (*e*) A–300/KCl (6 : 1) at h = 0.1 g/g and C_d = 0.2 g/g in $CDCl_3$ medium; and (*f*) A–300/LiCl (1 : 1) at h = 0.1 g/g and C_d = 0.15 g/g in $CDCl_3$ medium

On the NMR measurements, the predominantly hydrophobic character of polymeric adsorbent LiChrolut EN [16] caused incomplete filling of pores by water at the hydration degree h = 2 g/g. The amounts of bound water correspond to V_w = 0.73 cm^3/g (estimated from the amount of unfrozen water (C_{uw}) at 273 K) which is smaller than V_p = 0.83 cm^3/g but larger than that on the water vapor adsorption (30.44 mmol/g or 0.548 cm^3/g assuming that the density of bound water ρ_0 = 1 g/cm^3) at p/p_0 ≈ 1. The adsorbent is composed of main two structures with crosslinked [–CH–CH_2–Ph–CH–CH_2–]$_n$ (DVB) and linear [Ph(CH_2CH_3)–CH–CH_2–]$_m$ (EVB) chains and includes oxygen-containing groups at the end of the chains (because on free-radical polymerization of PSD and DVB activated by peroxides, growth of the chain occurs from the opposite end to peroxide); *i.e.*, the number of polar active sites in LiChrolut EN is relatively low. Therefore, dispersive interactions of water with the pore wall surface are predominant similar to that for carbon adsorbents which, however, are characterized by much higher ordering of condensed aromatic rings in basal planes [16, 59, 60] than LiChrolut EN adsorbent (upfield displacement of the spectra is not observed in contrast to that for carbon adsorbent C–47 (Fig. 22)).

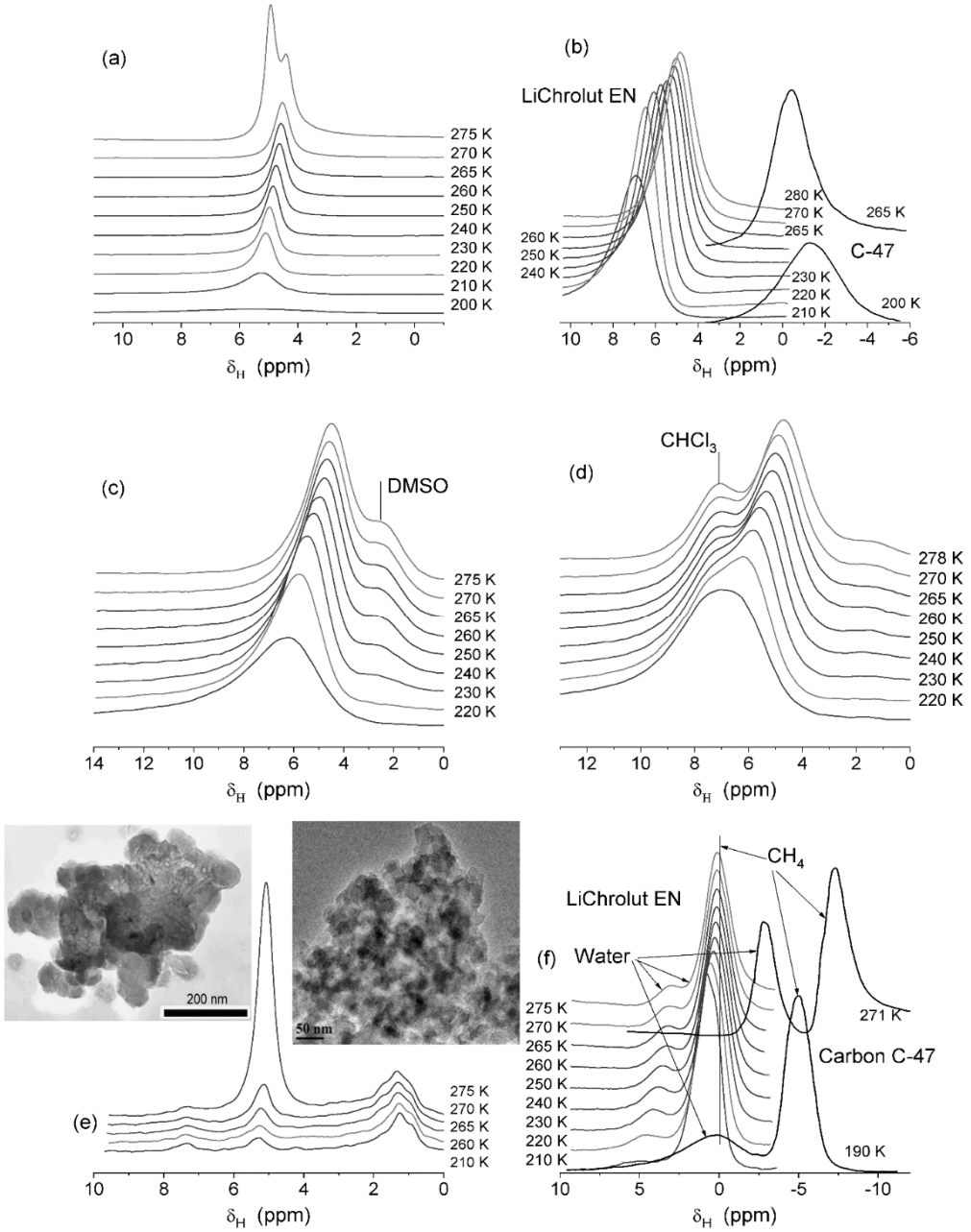

Fig. 22. ^{1}H NMR spectra of water bound to LiChrolut EN adsorbent at hydration h = (*a*) 2 and (*b*) 0.25 g/g and binding of water (pre–sorbed at h = (*c*, *d*, *f*) 0.25 and (*e*) 0.175 g/g) and organics (*c*) 20 wt. % of DMSO (half DMSO–d_6); (*d*) 30 wt. % of $CHCl_3$; (*e*) in the $CDCl_3$ medium; and (*f*) 10 wt. % of methane, hydrated activated carbon adsorbent C–47 at h = 4.71 g/g (*b*) and $h \approx 0.1$ g/g and adsorbed CH_4 (*f*) recorded at different temperatures (insert: TEM images of (left) LiChrolut EN, scale bar 200 nm, and (right) activated carbon, scale bar 50 nm)

The ^{1}H NMR spectra of water (h = 2 g/g) bound to LiChrolut EN are characterized by two signals at $T > 273$ K (δ_H = 5 and 4.5 ppm) and a single signal at $T < 273$ K with downfield shifts with lowering temperature (Fig. 22 *a*). Consequently, the shielding effect of π–electrons of aromatic rings (observed, *e.g.*, in micropores of carbon adsorbents as a significant upfield displacement of the ^{1}H NMR signal (Fig. 22 *b*)) on water bound in narrow pores of LiChrolut EN is very weak because of orientation disordering of neighboring aromatic rings, which do not form the condensed system as in carbon adsorbents. The signal at δ_H = 5 ppm can be attributed to water located out of pores (the amount

of water is greater than the pore volume) because it is frozen at 273 K. The second signal can be assigned to strongly associated water, which includes SBW and WBW fractions. In the case of partial infilling (approximately 30 % V_p) of pores, the water state changes (Fig. 22 *b*) in comparison with that on nearly completely infilling (~90 %) of pores (Fig. 22 *a*). An increase in the chemical shift δ_H is observed with decreasing temperature. Moreover at 210 K, the δ_H value is equal to 6.9 ppm close to the limiting value (7 ppm) for ice. This can be due to formation of ordered ice crystallites in pores with hydrophobic polymer walls. Notice that all water upon 30 % infilling of pores is SBW at $\Delta G < -2$ kJ/mol and located only in pores.

Added polar DMSO (20 wt. % with respect to the weight of dry polymer sample) (Fig. 22 *c*) or weakly polar $CHCl_3$ (30 wt. %) (Fig. 22 *d*) weakly influences the δ_H value of bound water. This could be due to location of water and organic phases in different pores with very low contact area between two liquids. For chloroform poorly water–soluble, this effect is typical and, therefore, can be expected. However, for DMSO well water-soluble, it would be possible to expect the formation of a homogeneous mixture with bound water (the sample after addition of DMSO was shaken and equilibrated before the measurements) at an intermediate δ_H value between 3 ppm (water dissolved in DMSO) and 5 ppm (strongly associated water alone). However, only strongly associated water is observed for this mixture (Fig. 22 *c*). Similar effects were previously observed for the water/organic mixtures bound to carbon and oxide adsorbents [16]. In the presence of $CHCl_3$ (Fig. 22 *c*) a portion of water transforms from SAW into WAW. If the chloroform amount is larger than the pore volume that a significant portion of water becomes WAW, and certain amount of water corresponds to WBW because it is frozen at temperatures close to 273 K (Fig. 22 *e*). This occurs because chloroform can displace a portion of water from narrow pores toward broader ones, and similar effects were observed for other adsorbents because of several reasons: (i) diminution of contact area of practically immiscible liquids (water and chloroform); (ii) weakly polar chloroform provides stronger dispersive interaction with hydrophobic pore walls of LiChrolut EN than polar water molecules; (iii) small water clusters (as WAW) remain in pores at oxygen-containing sites. In the ^{1}H NMR spectra besides the signal of SAW ($\delta_H \approx 5$ ppm), with intensity rapidly decreasing with decreasing temperature, the signal of WAW is observed at $\delta_H \approx 1.3$ ppm. The intensity of the latter depends weakly on temperature. A relatively complex shape of the ^{1}H NMR spectra of WAW can be due to different values of the magnetic susceptibility of adsorbates locating in pores of various sizes and the orientation effects of benzene rings (*i.e.*, local currents of π–electrons) in these pores.

On co-sorption of water and methane, the ^{1}H NMR spectra strongly change (Fig. 22 *b*, *f*) because of contribution of methane and possible changes in the location and state of bound water. The signal intensity of SAW decreases and WAW appears. A residual quantity of SAW corresponds to not more than 25 % of the initial one. The adsorption of methane is relatively high (up to 10 wt. %) because of a significant contribution of nanopores (incompletely infilled by water) of a complicated shape in LiChrolut EN adsorbent. The signals of WAW and methane overlap but at $T < 220$ K a clearly visible shoulder related to the methane signal appears at $\delta_H \approx 0$ ppm. On co-adsorption of water and methane, transition of water from SAW into WAW is thermodynamically preferable because water and methane can form the hydrate system stabilized in narrow pores of the adsorbent. Probably, the main reasons responsible for the formation of such structures is the topological characteristics of polymeric pores and the chemical structure of their walls with a low content of polar adsorption sites. The shielding effects of π–electrons of disordered benzene rings on sorbed water/methane mixture are much smaller for LiChrolut EN than that of ordered condensed benzene rings in carbon adsorbent C–47 (Fig. 22 *f*) since for two adsorbents $|\Delta\delta_H| >$ 5–7 ppm, which increases with temperature [16]. The associativity of water molecules depends on the presence of co-sorbate. For instance, bound water alone can be assigned to SAW (Fig. 22 *a*) because $\delta_H > 4$ ppm over the total temperature range. When the amount of bound water corresponds to approximately 30 % of the pore volume, co-adsorption of water and weakly polar chloroform causes the appearance of WAW.

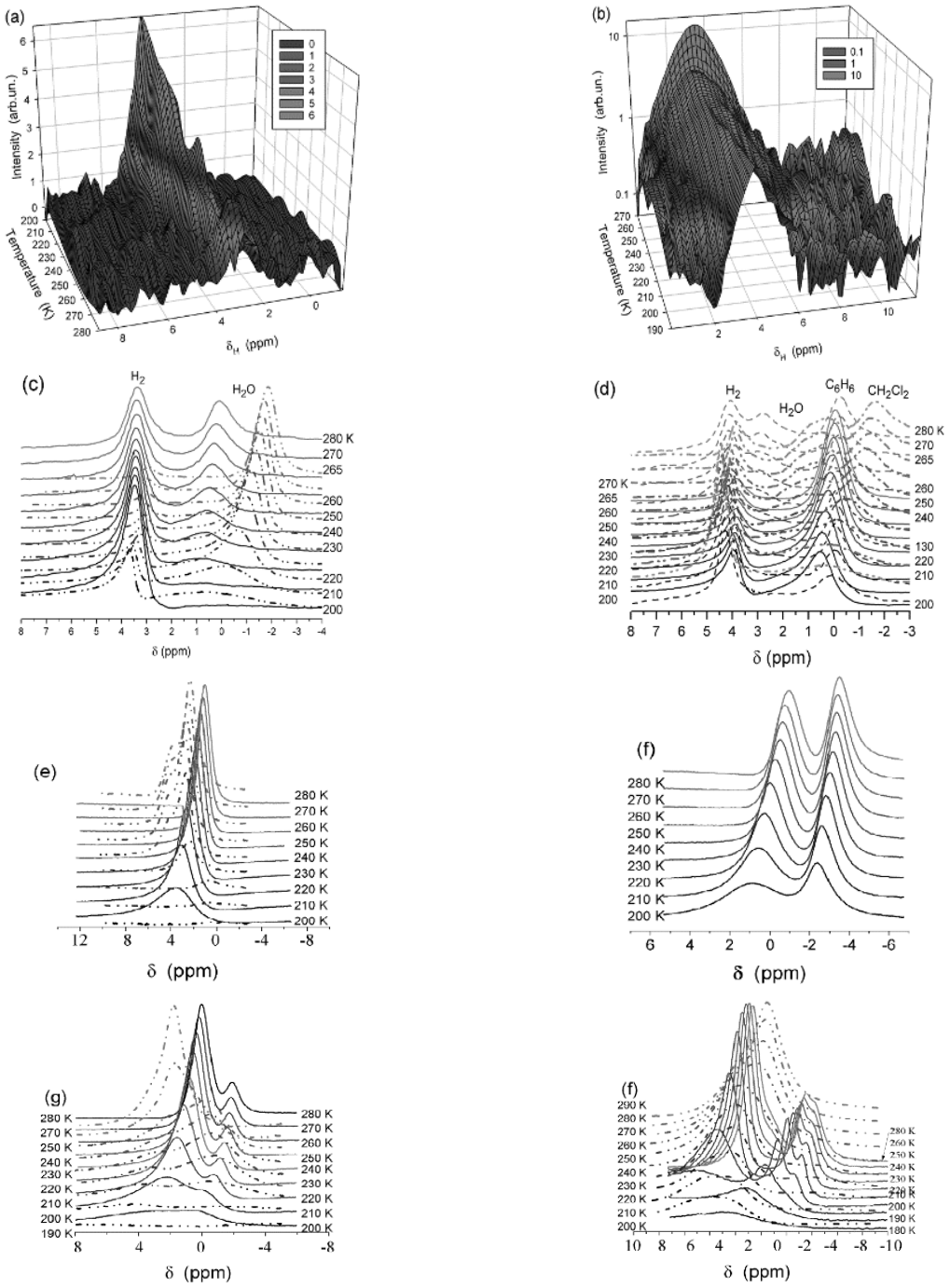

Fig. 23. ^{1}H NMR spectra of hydrogen bound to silicalite (*a*) dry and (*b*) hydrated (h = 0.02 g/g); hydrogen and water co-sorbed onto C–86 at (*c*) h = 0.002 g/g (solid lines) and 0.04 g/g (dotted–dashed lines); (*d*) with the presence of benzene (0.03 g/g) (solid lines), benzene (0.0075 g/g) and water (0.001 g/g) (dashed), and water (0.001 g/g) and CH_2Cl_2 (0.0085 g/g) (dotted-dashed); water (h = 0.1 g/g) sorbed on C–47 in mixtures with (*e*) CD_3CN at 0.1 g/g (solid lines) and 2 g/g (dotted–dashed); (*f*) $(CH_3)_2CO$ (0.1 g/g); (*g*) $(CD_3)_2SO$ at 0.1 g/g (solid lines) and 2 g/g (dotted-dashed); and (*h*) $(CH_3)_2SO$ at 0.1 g/g (solid lines) and 2 g/g (dotted–dashed lines)

Competitive sorption of water, light gases, and organic liquids are strongly affected by the sorbent characteristics, content of sorbates, and temperatures (Fig. 23) due to variations in the CSE and CE. For hydrogen and methane, pre-sorbed water effects could be textural (changes in

effective porosity with increased contribution of narrower pores appropriate for adsorption of H_2 (Fig. 23 *a*, *b*) and CH_4, trapping, and hydrate formation. The latter is less possible than the first two effects because maximal pressure could be provided in nanopores where the hydrate cells could not be formed due to steric effects. Even in the case of AC with high contribution of nanopores, great SSA and V_p, bound water can positively affect the hydrogen adsorption, but increasing water content results in diminution of hydrogen adsorption (Fig. 23 *c*). Not only bound water can affect the adsorption of light gases, but also other liquids with relatively small molecules (*e.g.*, C_6H_6 and CH_2Cl_2) (Fig. 23 *d*). Co-sorption of organics and water can be used for more complete control of the adsorption of light gases (Fig. 23 *d*) because competitive sorption of water and organics (Fig. 23 *e*–*h*) results in certain changes in effective texture of sorbents that become better for light gases adsorption. Bound solvents located in narrower pores possess lower activity than that located in broader pores or in the bulk. This is due to strong interactions of molecules with sorbents that result in decreased mobility of molecules, changes in their organization in smaller clusters due to spatial restrictions. The formation of solvation shells in narrower pores is less possible than in broader ones.

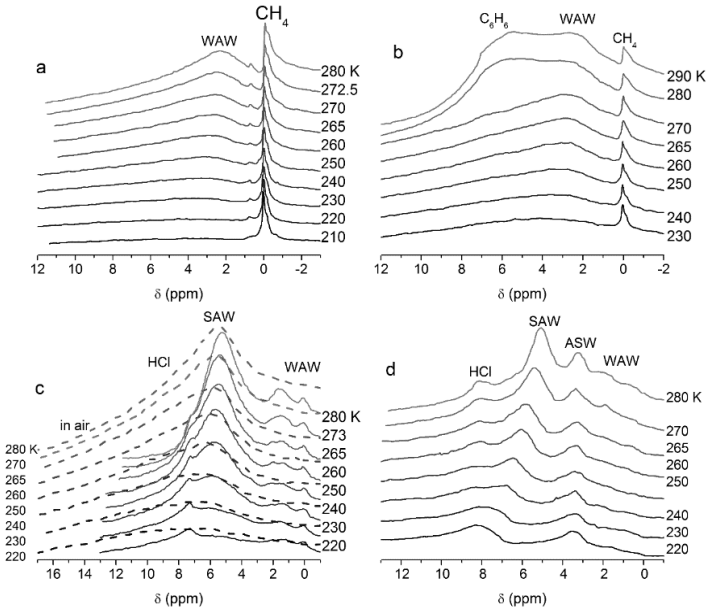

Fig. 24. ^{1}H NMR spectra of water bound to MLGO at hydration h = (*a*, *b*) 0.1, (*c*) 0.3 and (*d*) 0.5 g/g with co-sorbed (*a*, *b*) methane (from reservoir at pressure of 1.1 bar), (*b*) +1 g/g benzene; (*c*) 0.1 g/g HCl in air (dashed lines) or $CDCl_3$ (solid lines) dispersion medium; and (*d*) 0.2 HCl (in $CDCl_3$+DMSO medium)

The spectral characteristics of water bound to multi-layer graphene oxide (MLGO) [68] did not change in the methane atmosphere (Fig. 24 *a*) because the CH_4 adsorption was low (< 1 wt. %) since the volume of nanopores in MLGO is small. The spectra of co-sorbed water and benzene (Fig. 24 *b*) include intensive broad signal of benzene (melting point 278.7 K) at T > 270 K. Consequently, its freezing temperature is only slightly decreased versus the bulk solvent. This is due to weak interactions of benzene molecules with a strongly oxidized surface of MLGO. The spectra of the bound HCl solution depends on both co-sorbates content and the type of dispersion medium (Fig. 24 *c*, *d*). An increase in the quantity of water and HCl and replacement of air by chloroform alone or in a mixture with DMSO leads to the appearance of a signal at 9 ppm, which is characteristic for a concentrated HCl solution. The downfield shift is observed with decreasing temperature due to two effects: (i) concentrating HCl solution in SAW, and (ii) stronger interactions of layers located close to the surface with the surface O–functionalities. In the $CDCl_3$ medium, the spectra change (Fig. 24 *c*, *d*). The main signal demonstrates upfield shift (by 0.5 ppm). The signal of the concentrated HCl solution ($\delta_H \approx 9$ ppm) is not observed but a signal

of WAW appears at $\delta_H \approx 1.5$ ppm. An increase in the dispersion medium polarity by addition of 10 % of DMSO results in more complex spectra (Fig. 24 *d*) including 4–5 signals. For example, the signal of water associated with DMSO molecules (ASW) at $\delta_H \approx 3.5$ ppm does not change the position in contrast to a signal of SAW at $\delta_H \approx 5$ ppm at 280 K (with a small portion of dissolved HCl) and 7 ppm at 240 K. The latter is due to changes in the content of HCl in SAW at decreasing temperature because of acid concentrating effect. Therefore, only one signal ($\delta_H \approx 8.5$ ppm) of HCl/SAW is observed at 220 K due to summarized CSE + CE influence, however, it does not correspond to complete synergetic (CSE+CE) effect. In contrast to SAW, WAW cannot dissolve HCl. Therefore, the signal position of WAW at $\delta_H \approx 1.5$ ppm does not change with decreasing temperature.

CONCLUSION

Confined space effects lead to the freezing point depression and can affect the colligative properties of liquid mixtures with respect to FPD at $T < T_{f,b}$. For some systems with maximal FPD due to cryscopic effects for bulk non–ideal solutions, there is no complete additivity of CSE and CE:

$FPD_{CSE} < FPD_{CSE+CE} < FPD_{CE,b}$ and $|\Delta G_{CSE+CE}| < |\Delta G_{CSE}|+|\Delta G_{CE,b}|$.

However, for some others with minimal FPD for bulk almost ideal solutions, there is significant additivity of CSE and CE, *i.e.*, there are the synergetic effects (which, however, is not observed for total amounts of bound mixtures):

$FPD_{CE,b} < FPD_{CSE} < FPD_{CSE+CE}$ and $|\Delta G_{CE,b}|<|\Delta G_{CSE}|<|\Delta G_{CSE+CE}|$.

This occurs due to several factors:

- changes in the concentrations of liquids (solvents and solutes) in the mixtures;
- spatial restrictions for the formation of complete solvation shells in narrow pores;
- decrease in the solvation activity of any solvent located in narrow pores;
- stronger decrease in molecular mobility in narrower pores affected by topological nonuniformities of pores and pore walls;
- differentiation and structurization of the liquid phases of the mixtures located in pores;
- clusterization of molecules around strong adsorption sites;
- effects of dispersion media with or without mixing with solvents or solutes;
- displacement of a solvent (*e.g.*, water) toward broader or narrower pores by immiscible liquid from dispersion media.

As one of consequences of the obtained results, corrected cryoporometry equation should be used for the mixtures:

$$\Delta T_{f,CSE} - \alpha \Delta T_{f,CE/CSE} = -k/R,$$

where α is the structural factor affected by CSE, $\alpha < 1$ for miscible compounds (*e.g.*, acids, NaOH, DMSO with water) and $\alpha = 0$ for immiscible ones (*e.g.*, water and *n*-decane or chloroform). Pore size decrease leads to an increase in CSE and a decrease in CE. This approach allows one to study the organization of various mixtures in pores. As a whole, there is no complete additivity of CSE and CE because CSE lead not only to the freezing point depression but also diminution in the activity of solvents up to phase separation.

The obtained results and analysis are of interest from both practical and theoretical point of view. In future, it could be interesting to study a set of systems with different materials (*e.g.*, silica and carbons) possessing various porosity at a wide range of solute concentrations.

ACKNOWLEDGEMENTS

The authors are grateful to the National Research Foundation of Ukraine (Support of advanced and young scientists, grant 2020.02/0057) for financial support of this study. V.M.G. is grateful to Gaussian, Inc. for the Gaussian 16, Revision C.02. The authors thank Dr. I. Protsak, Dr. E. Pakhlov, Dr. L. Andriyko, Dr. T. Krupska (CISC), and Dr. hab. B. Charmas (MCSU) for some experimental data.

Колігативні властивості різних рідких сумішей в залежності від температури та ефектів обмеженого простору у порах різних адсорбентів

В.М. Гунько, В.В. Туров

Інститут хімії поверхні ім. О.О. Чуйка Національної академії наук України
вул. Генерала Наумова, 17, Київ, 03164, Україна, vlad_gunko@ukr.net

Температура і межфазна поведінка окремих і змішаних рідин важливі з практичної точки зору, оскільки зміни фазового стану сполук при зниженні температури можуть призвести до негативних наслідків (наприклад, пошкодження пористих матеріалів при низьких температурах). Однак використання певних сумішей могло б запобігти цим ефектам завдяки колігативним властивостям розчинів. Ефекти обмеженого простору (CSE), що призводять до зниження точки замерзання (FPD), можуть впливати на колігативні властивості рідких сумішей щодо FPD. Можна припустити, що для деяких систем з певним FPD через кріоскопічні ефекти (CE) для розчинів немає адитивності CSE та CE, але для інших можуть бути протилежні результати. Щоб з'ясувати ці міжфазні явища, було досліджено набір рідких сумішей, пов'язаних з різними адсорбентами, за допомогою низькотемпературної ЯМР–спектроскопії. Ці розчини включають кислоти, основи та солі як розчинені речовини, деякі рідини (наприклад, диметилсульфоксид, ацетонітрил, декан) як ко–сорбати та інші (наприклад, $CDCl_3$, CCl_4) як дисперсійні середовища. Як адсорбенти досліджували різні пористі та високодисперсні кремнеземи, пірогенний оксид алюмінію, вуглецеві матеріали (активоване вугілля, оксиди графену) та пористі полімери. Широкий діапазон досліджуваних систем може дозволити глибше зрозуміти конкурентоспроможні чи адитивні CSE та CE, що впливають на міжфазну та температурну поведінку зв'язаних рідин. Результати цього аналізу становлять інтерес як з практичної, так і з теоретичної точок зору.

***Ключові слова**: нанокремнезем, силікагель, вуглецеві адсорбенти, полімерні адсорбенти, зв'язані водні розчини, явища на межах поділу, ефекти обмеженого простору, кріоскопічні ефекти*

REFERENCES

1. Franks F. *Biophysics and Biochemistry at Low Temperatures*. (Cambridge: Cambridge University Press. 1985).
2. Konsta–Gdoutos M.S. (editor). *Measuring, Monitoring and Modeling Concrete Properties*. (Dordrecht: Springer, 2006).
3. Grout B.W.W., Morris G.J. (editors). *The Effects of Low Temperatures on Biological Systems*. (London: Edward and Arnold Publishers. 1987).
4. Kamide K. Colligative properties. *Comprehensive Polymer Science and Supplements*. 1989. **4**: 75.
5. Kamide K., Dobashi T. *Physical Chemistry of Polymer Solutions. Theoretical Background*. (Elsevier, 2000).
6. Reuter J.H., Perdue E.M. Calculation of molecular weights of humic substances from colligative data: Application to aquatic humus and its molecular fractions. *Geochim. Cosmochim. Acta.* 1981. **45**(11): 2017.
7. Stepanos J.J., Addison A.W. *Chemical Thermodynamics and Statistical Aspects: Questions to Ask in Fundamentals and Principle*. (Elsevier, 2023).
8. Mazza D., Canuto E. *Fundamental Chemistry with Matlab*. (Elsevier, 2022).
9. Gaffney J.S., Marley N.A. *General Chemistry for Engineers*. (Elsevier, 2018).
10. DeVoe H. *Thermodynamics and Chemistry, LibreTexts, Chemistry*. (California State University, 2022).
11. Pancerz M., Ptaszek A., Sofińska K., Barbasz J., Szlachcic P., Kucharek M., Łukasiewicz M. Colligative and hydrodynamic properties of aqueous solutions of pectin from cornelian cherry and commercial apple pectin. *Food Hydrocolloids.* 2019. **89**: 406.
12. Gonda I., Groom C.V. Colligative properties of disodium cromoglycate aqueous solutions in relation to their phase diagram. *J. Colloid Interface Sci*. 1983. **92**: 289.
13. Nagvekar M., Tihminlioglu F., Danner R.P. Colligative properties of polyelectrolyte solutions. *Fluid Phase Equilibria*. 1998. **145**(1): 15.
14. Mjallal I., Feghali E., Hammoud M., Habchi C., Lemenand T. Exploring the colligative properties of Arachidic acid for potential use as PCM. *Solar Energy.* 2021. **214**: 19.
15. Kimmich R. *NMR Tomography, Diffusometry, Relaxometry*. (Heidelberg: Springer, 1997).

16. Gun'ko V.M., Turov V.V. *Nuclear Magnetic Resonance Studies of Interfacial Phenomena*. (Boca Raton: CRC Press, 2013).
17. Petrov O.V., Furó I. NMR cryoporometry: Principles, applications and potential. *Prog. Nuclear Magn. Reson. Spectr*. 2009. **54**(2): 97.
18. Mitchell J., Webber J.B.W., Strange J.H. Nuclear magnetic resonance cryoporometry. *Phys. Rep*. 2008. **461**(1): 1.
19. Chaplin M. *Water structure and science*. http://www1.lsbu.ac.uk/water/, accessed on 2 October, 2023.
20. Rasmussen D.H., MacKenzie A.P. Phase diagram for the system water–dimethylsulphoxide. *Nature*. 1968. **220**: 1315.
21. *Technical Bulletin Reaction Solvent Dimethyl Sulfoxide* (105B DMSO). Gaylord Chemical. 2011. 105FINALnoframe2.doc (chemistry–chemists.com).
22. Lam S.Y., Benoit R.L. Some thermodynamic properties of the dimethylsulfoxide–water and propylene carbonate–water systems at 25 °C. *Can. J. Chem*. 1974. **52**(5): 718.
23. Lü P., Zhao G., Zhang X., Yin J., Bao J. Measurement and prediction on the surface properties of dimethyl sulfoxide/water mixtures. *Chem. Res. Chin. Univ.* 2016. **32**: 100.
24. Mohan G., Venkataraman M., Gomez–Vidal J., Coventry J. Assessment of a novel ternary eutectic chloride salt for next generation high–temperature sensible heat storage. *Energy Conversion and Management*. 2018. **167**: 156.
25. Viola W., Andrew T.L. An aqueous eutectic electrolyte for low–cost, safe energy storage with an operational temperature range of 150 °C, from –70 to 80 °C. *J. Phys. Chem. C*. 2021. **125**(1): 246.
26. Barnes W.H., Maass O. Freezing points and heat capacities of aqueous solutions of potassium chloride. *Can. J. Res*. 1930. **2**(3): 218.
27. Harriss M.G., Milne J.B. The trifluoroacetic acid solvent system. Part V. Cryoscopic measurements. *Can. J. Chem*. 1976. **54**(19): 3031.
28. Haghighi H., Chapoy A., Tohidi B. Freezing point depression of electrolyte solutions: experimental measurements and modeling using the cubic–plus–association equation of state. *Ind. Eng. Chem. Res*. 2008. **47**(11): 3983.
29. Cady H.H., Cady G.H. Freezing points of the system water–trifluoroacetic acid. *J. Am. Chem. Soc*. 1954. **76**(3): 915.
30. Zavitsas A.A. Some opinions of an innocent bystander regarding the Hofmeister series. *Current Opinion Colloid Interface Sci.* 2016. **23**: 72.
31. Wang G., Zhou Y., Jing Z., Wang Y., Chai K., Liu H., Zhu F., Wu Z. Anomalous ion hydration and association in confined aqueous $CaCl_2$ solution. *J. Mol. Liquid.* 2022. **360**: 119409.
32. Petroselli M., Chen Y.–Q., Zhao M.–K., Rebek J. Jr., Yu Y. C–H...X–C bonds in alkyl halides drive reverse selectivities in confined spaces. *Chinese Chemical Letters*. 2023. **34**(5): 107834.
33. Malfait B., Jani A., Morineau D. Confining deep eutectic solvents in nanopores: Insight into thermodynamics and chemical activity. *J. Mol. Liquid.* 2022. **349**: 118488.
34. Gun'ko V.M., Turov V.V., Krupska T.V., Borysenko M.V. Surroundings effects on the interfacial and temperature behaviors of NaOH/water bound to hydrophilic and hydrophobic nanosilicas. *J. Colloid Interface Sci*. 2023. **634**: 93.
35. Gun'ko V.M., Turov V.V., Pakhlov E.M., Krupska T.V., Charmas B. Effect of water content on the characteristics of hydro–compacted nanosilica. *Appl. Surf. Sci*. 2018. **459**: 171.
36. Gun'ko V.M., Turov V.V., Goncharuk O.V., Pakhlov E.M., Matkovsky O.K. Interfacial phenomena at a surface of individual and complex fumed nanooxides. *Surface*. 2019. **11(26)**: 3.
37. Gun'ko V.M., Turov V.V., Zarko V.I., Goncharuk E.V., Gerashchenko I.I., Turova A.A., Mironyuk I.F., Leboda R., Skubiszewska–Zięba J., Janusz W. Comparative characterization of polymethylsiloxane hydrogel and silylated fumed silica and silica gel. *J. Colloid Interface Sci*. 2007. **308**(1): 142.
38. Gun'ko V.M., Turov V.V., Krupska T.V., Protsak I.S., Borysenko M.V., Pakhlov E.M. Polymethylsiloxane alone and in composition with nanosilica under various conditions. *J. Colloid Interface Sci*. 2019. **541**: 213.
39. Gun'ko V.M., Turov V.V. Nanostructured systems based on polymethylsiloxane and nanosilicas with hydrophobic and hydrophilic functionalities. *Colloids Surf. A*. 2023. **677**: 132448.
40. Collins K.D. Ions from the Hofmeister series and osmolytes: Effects on proteins in solution and in the crystallization process. *Methods*. 2004. **34**(3): 300.
41. Robinson J.B. Jr., Strottmann J.M., Stellwagen E. *Proc. Natl. Acad. Sci. USA*. 1981. **78**: 2287.
42. Gupta S., Pel L., Kopinga K. Crystallization behavior of NaCl droplet during repeated crystallization and dissolution cycles: An NMR study. *J. Crystal Growth*. 2014. **391**: 64.
43. Mallamace F., Corsaro C., Broccio M., Branca C., González–Segredo N., Spooren J., Chen S.–H., Stanley H.E. NMR evidence of a sharp change in a measure of local order in deeply supercooled confined water. *Proc. Natl. Acad. Sci. USA*. 2008. **105**(35): 12725.
44. Gregg S.J., Sing K.S.W. *Adsorption, Surface Area and Porosity*. 2nd ed. (London: Academic Press, 1982).
45. Adamson A.W., Gast A.P. *Physical Chemistry of Surface*. Sixth edn. (New York: Wiley, 1997).
46. Gun'ko V.M. Textural characteristics of composite adsorbents analyzed with density functional theory and self–consistent regularization procedure. *Him. Fiz. Tehnol. Poverhni.* 2020. **11**(2): 163.

47. Frisch M.J., Trucks G.W., Schlegel H.B., Scuseria G.E., Robb M.A., Cheeseman J.R., Scalmani G., Barone V., Petersson G.A., Nakatsuji H., Li X., Caricato M., Marenich A.V., Bloino J., Janesko B.G., Gomperts R., Mennucci B., Hratchian H.P., Ortiz J.V., Izmaylov A.F., Sonnenberg J.L., Williams–Young D., Ding F., Lipparini F., Egidi F., Goings J., Peng B., Petrone A., Henderson T., Ranasinghe D., Zakrzewski V.G., Gao J., Rega N., Zheng G., Liang W., Hada M., Ehara M., Toyota K., Fukuda R., Hasegawa J., Ishida M., Nakajima T., Honda Y., Kitao O., Nakai H., Vreven T., Throssell K., Montgomery J.A. Jr., Peralta J.E., Ogliaro F., Bearpark M.J., Heyd J.J., Brothers E.N., Kudin K.N., Staroverov V.N., Keith T.A., Kobayashi R., Normand J., Raghavachari K., Rendell A.P., Burant J.C., Iyengar S.S., Tomasi J., Cossi M., Millam J.M., Klene M., Adamo C., Cammi R., Ochterski J.W., Martin R.L., Morokuma K., Farkas O., Foresman J.B., Fox D.J. Gaussian 16, Revision C.02, Gaussian, Inc., Wallingford CT, 2019.
48. Barca G.M.J., Bertoni C., Carrington L., Datta D., De Silva N., Deustua J.E., Fedorov D.G., Gour J.R., Gunina A.O., Guidez E., Harville T., Irle S., Ivanic J., Kowalski K., Leang S.S., Li H., Li W., Lutz J.J., Magoulas I., Mato J., Mironov V., Nakata H., Pham B.Q., Piecuch P., Poole D., Pruitt S.R., Rendell A.P., Roskop L.B., Ruedenberg K. Recent developments in the general atomic and molecular electronic structure system. *J. Chem. Phys.* 2020. **152**(15): 154102.
49. Marenich A.V., Cramer C.J., Truhlar D.G. Universal solvation model based on solute electron density and on a continuum model of the solvent defined by the bulk dielectric constant and atomic surface tensions. *J. Phys. Chem. B* 2009. **113**(18): 6378.
50. Stewart J.J.P. MOPAC2022. Stewart Computational Chemistry. web: HTTP://OpenMOPAC.net. 2022. (accessed on 06.12.2022).
51. Pettersen E.F., Goddard T.D., Huang C.C., Meng E.C., Couch G.S., Croll T.I., Morris J.H., Ferrin T.E. UCSF ChimeraX: Structure visualization for researchers, educators, and developers. *Protein Sci.* 2021. **30**(1): 70.
52. *Avogadro 2*. https://two.avogadro.cc/. Ver. 1.97. 2023.
53. Zhurko G.A., Zhurko D.A. *Chemcraft* (version 1.8, build 640). http://www.chemcraftprog.com.
54. *Jmol: an open–source Java viewer for chemical structures in 3D* (Ver. 16.1.41). http://www.jmol.org/.
55. Thommes M., Kaneko K., Neimark A.V., Olivier J.P., Rodriguez–Reinoso F., Rouquerol J., Sing K.S.W. Physisorption of gases, with special reference to the evaluation of surface area and pore size distribution. IUPAC Technical Report. *Pure Application Chemistry.* 2015. **87**(9–10): 1051.
56. Gregg S.J., Sing K.S.W., Stoeckli H.F. (editors). *Characterization of Porous Solids*. (London: Soc. Chem. Industry, 1979).
57. Rouquerol J., Baron G.V., Denoyel R., Giesche H., Groen J., Klobes P., Levitz P., Neimark A.V., Rigby S., Skudas R., Sing K., Thommes M., Unger K. The characterization of macroporous solids: An overview of the methodology. *Microporous Mesoporous Mater*. 2012. **154**: 2.
58. Shegokar R., Souto E.B. (editors), *Characterization of Micro and Nanoparticles for Biomedical Applications* (Micro and Nano Technologies). (Elsevier, 2024. ISBN: 9780323961387).
59. McEnaney B., Mays T.J., Rodriguez–Reinoso F. (editors). *Fundamental Aspects of Active Carbons*. Special issue. *Carbon* 1998. **36**(10).
60. Cooney D.O. *Activated Charcoal in Medical Applications*. (New York: Marcel Dekker, 1995).
61. Rodriguez–Reinoso F., McEnaney B., Rouquerol J., Unger K. (editors). *Studies in Surface Science and Catalysis.* V. 144, *Characterisation of Porous Solids VI*. (Amsterdam: Elsevier Science, 2002).
62. Biricik H., Sarier N. Comparative study of the characteristics of nano silica–, silica fume– and fly ash – incorporated cement mortars. *Materials Research.* 2014. **17**(3): 570.
63. Hashim A.A. (editor). *Smart Nanoparticles Technology*. (Rijeka, Croatia: InTech, 2012).
64. Iler R.K. *The Chemistry of Silica. Solubility, Polymerization, Colloid and Surface Properties, and Biochemistry*. (Chichester: Wiley, 1979).
65. Bergna H.E., Roberts W.O. (editors). *Colloidal Silica: Fundamentals and Applications*. (Boca Raton: CRC Press, 2006).
66. Legrand A.P. (editor). *The Surface Properties of Silicas*. (New York: Wiley, 1998).
67. *Basic characteristics of Aerosil fumed silica* (4th ed.). Tech. Bull. Fine Particles 11. (Hanau: Evonik Industries, 2014).
68. Gun'ko V.M., Turov V.V., Zarko V.I., Goncharuk O.V., Matkovsky A.K., Prykhod'ko G.P., Nychiporuk Yu.M., Pakhlov E.M., Krupska T.V., Balakin D.Yu., Charmas B., Andriyko L.S., Skubiszewska–Zięba J., Marynin A.I., Ukrainets A.I., Kartel M.T. Multi–layer graphene oxide alone and in a composite with nanosilica: preparation and interactions with polar and nonpolar adsorbates. *Applied Surface Science*. 2016. **387**: 736.

Received 25.10.2023, accepted 19.02.2024